Zone Plate Array Lithography (ZPAL): Simulations and System Design

by

Rajesh Menon

Submitted to the Department of Electrical Engineering and Computer Science
in partial fulfillment of the requirements for the degree of

Master of Science in Electrical Engineering and Computer Science

at the

MASSACHUSETTS INSTITUTE OF TECHNOLOGY

June 2000

Author .....
Department of Electrical Engineering and Computer Science
May 8, 2000

Certified by .....
Henry I. Smith
The Joseph F. and Nancy P. Keithley Professor of Electrical Engineering
Thesis Supervisor

Accepted by .....
Arthur C. Smith
Chairman, Department Committee on Graduate Students

Zone Plate Array Lithography (ZPAL): Simulations and System Design

by

Rajesh Menon

Submitted to the Department of Electrical Engineering and Computer Science
on May 8, 2000, in partial fulfillment of the
requirements for the degree of
Master of Science in Electrical Engineering and Computer Science

Abstract

The semiconductor industry has been the driving force behind the information revolution witnessed in the last few decades. One could make a credible claim that lithography is the backbone upon which this industry is built up. In order to sustain this exponential growth, the requirements for lithographic tools are becoming incredibly complex and expensive. Clearly, there is a need for a fresh approach to lithography. Zone-Plate-Array Lithography (ZPAL) was proposed to provide this paradigm shift and satisfy all the requirements for the present, as well as the future, in a simple and elegant manner.

An analytical study of the effect of the various parameters in a ZPAL system on the lithographic figures-of-merit is described in this thesis. A simulation tool was built to examine the diffraction properties of zone plates based on scalar diffraction theory. The effects of various system parameters such as the zone plate geometry and the source characteristics are discussed. Simulated patterns are compared to patterns that were exposed in resist using an in-house UV ZPAL system. The simulation tool showed excellent agreement with the experimental results. Since the size of the source is an important issue in x-ray ZPAL, a simulation tool based on classical electrodynamics was built to study the characteristics of an electron-bombardment x-ray source. This tool was used to propose an improved design for the source.

Thesis Supervisor: Henry I. Smith
Title: The Joseph F. and Nancy P. Keithley Professor of Electrical Engineering

Acknowledgments

First and foremost, I would like to express my gratitude to Professor Hank Smith. I greatly admire his wonderful intuition and his capacity to envision unconventional ideas and pursue them with unbridled enthusiasm. I look forward to completing my graduate education under his supervision. The realization of ZPAL as a real lithographic tool would not have been possible without the relentless efforts of Dave Carter and Darío Gil. Dave is a remarkable combination of a scientist and an engineer. I have gained many ideas through our discussions. I would like to especially thank Dave for trying ever so hard to instill experimental skills in me. I would like to thank Darío for all the experimental results reported in this thesis. Our conversations on myriad topics have enriched me greatly. I cherish the friendship I share with him.

Several people have contributed in the realization of this project both directly and indirectly. Much of the work on the electron-bombardment x-ray source was done in collaboration with Alex Bernstein. I appreciate all his help and also his suggestions on writing this thesis in Latex. I would like to thank Tom Murphy for many engaging discussions and suggestions. Credit also goes to Tom for the wonderful network and computing support he provides. Kenichi Murooka's many helpful suggestions during the course of the project is greatly appreciated. I would like to extend my gratitude to Dave Foss for all the help and support he has provided me for running the programs on the IBM SP. Several students and staff at the NanoStructures laboratory including J. Ferrera, J. Hastings, E. Moon, P. Konkola, F. Zhang, M. Lim, M. Farhoud, T. Savas, D. Pflug, F. Rana, M. Walsh, J. Khan, M. Finlayson, J. Goodberlet, M. Schattenberg, M. Mondol and C. Lewis have contributed in several capacities to the success of this project. I would also like to express my appreciation for my wonderful friends. I have learnt a lot from my friend, Paul Herz. I fondly cherish our football games in Killian court, the snowboarding trip and sailing on the Charles. I also would like to appreciate the friendship of Joyce Wu, Mike Masaki, Juliet Gopinath, Samuel Mertens, Raj Vaidyanathan, Manish Bhardwaj, Noah Zamdmer, Hans Calebaut and many others. I have shared class and study times with many of them. Many thanks

goes to all my wonderful teachers from high school to college. I have learnt countless lessons from each and every one of them.

I would like to express my gratitude to my parents, who had more belief in my abilities than anyone else. I am ever grateful for their love. My sister, Rakhee and her husband, Vijay have been my closest family since I came to MIT. I thank them deeply for everything they have done for me. Last but not the least, I would like to thank Trina for being everything I wished for. She has enriched me in ways she doesn't realize herself. I am always grateful for the kind love and patience she has shown me.

ज्ञानेन तु तदज्ञानं येषां नाशितमात्मनः ।
तेषामादित्यवज्ज्ञानं प्रकाशयति तत्परम् ॥१६॥

"But of those whom this ignorance has been destroyed by the knowledge of the self; that knowledge is like the rising sun illuminated by the Ultimate Truth."

— Sri Krishna in Bhagwad Gita

Contents

1 Introduction to Zone-Plate-Array Lithography (ZPAL) 17

1.1 System Description 18

1.2 Development of the Project 19

1.3 Motivation for Simulations 20

2 Optical Properties of Zone Plates 23

2.1 Geometry and Optics 23

3 Diffraction by Zone Plates 35

3.1 Huygens-Fresnel Principle 35

3.2 Fresnel-Kirchhoff Diffraction Theory 38

3.3 Point-Spread Function Analysis for a Zone Plate 41

4 Numerical Simulations 45

4.1 Parallel Processing Concepts 46

4.2 Details of Hardware 48

4.3 Details of Software 48

4.4 Numerical Integration Issues 50

4.5 Timing Issues 53

5 Simulation Results 55

5.1 Diffraction Pattern in the Focal Plane 55

5.1.1 Effect of Zone Plate parameters 55

5.1.2 Effect of Source Parameters 62

5.2 Effects of Fabrication Errors 67
5.2.1 Zone Boundary Errors 67
5.2.2 Phase Shift Errors 69
5.3 Pattern Simulations 71
5.3.1 UV ZPAL Experimental Setup 72
5.4 Validation of Scalar Theory 81

6 X-ray Source Simulations **85**
6.1 Electron-bombardment x-ray Source 85
6.2 Electrodynamics 86
6.3 Simulation Results 89

7 Conclusions and Recommendations **97**

A Overview of System Software **99**

B X-ray Source Measurements **103**

List of Figures

1-1 A ZPAL system. 19

1-2 Overview of Simulations 21

2-1 Construction of a Zone Plate. 24

2-2 A Zone Plate. 25

2-3 Derivation of expressions for zone radii. 25

2-4 Non-existence of even order foci in zone plates 26

2-5 Zone plate radii 27

2-6 Possible zone plate designs 28

2-7 Optical path lengths 29

2-8 Existence of high order foci for high NA zone plates 30

2-9 Comparison of zone radii formulae 32

2-10 Zone plate showing ± 1 and ± 3 order radiation. 33

3-1 Derivation of the mathematical expression for Fresnel-Huygens Principle. 36

3-2 Illustration of the 3 different regions of diffraction. 37

3-3 Two closed surfaces around a point P where a spherical wavelet has a singularity. 39

3-4 Diffraction by an arbitrary aperture. 40

3-5 Fresnel-Kirchhoff diffraction for a zone plate. 42

4-1 Basic flow chart of the simulations. 45

4-2 Categories of processing schemes. 46

4-3 Parallelizing the problem 47

4-4 Study of convergence 52
4-5 Speedup versus number of processors for a representative problem . . 53

5-1 Point-spread function of a zone plate 56
5-2 Effect of N and f on FWHM 57
5-3 Different diffracted orders of a zone plate 58
5-4 Diffracted intensity in the focal plane for large radial distances 59
5-5 Effect of N and f on the efficiency 60
5-6 Effect of OZW on efficiency and FWHM 61
5-7 Axial intensity distribution for a zone plate 61
5-8 Effect of N and OZW on DOF 62
5-9 Building up a zone plate 63
5-10 Covering the zone plate with a central stop of increasing radius . . . 63
5-11 Image formation by a zone plate 65
5-12 Effects of a source of finite size 65
5-13 Effects of a source of finite bandwidth 66
5-14 Axial effects of a source of finite bandwidth 67
5-15 Effect of zone-boundary errors 68
5-16 Effect of zone-boundary error on the axial intensity distribution . . . 69
5-17 Effect of phase shift error 70
5-18 Simulating a pattern 72
5-19 A photograph of the UV ZPAL setup 73
5-20 Nine different patterns drawn in Nanowriter 74
5-21 Scanning electron micrographs (SEMs) of 9 different patterns written in parallel using UV ZPAL 75
5-22 Comparison of spot simulations to exposures 76
5-23 Comparison of pattern simulations to exposures 77
5-24 SEM of the x-ray amplitude zone plates 78
5-25 Simulations for x-ray amplitude zone plates 79
5-26 Pattern simulations for a 25 nm OZW zone plate 80

5-27 Outer zones of a zone plate 82
5-28 Refractive index profile of outer zones of a zone plate 83

6-1 X-ray emission by an electron bombarding a target atom 86
6-2 Electron-bombardment x-ray source 89
6-3 Computed fields for the existing x-ray source 90
6-4 Computed trajectories for the existing x-ray source 91
6-5 Two foci of the existing x-ray source 91
6-6 Electron counts for two foci 92
6-7 Design of improved x-ray source 93
6-8 Computed fields for the new x-ray source 94
6-9 Computed trajectories and electron distribution for the new x-ray source in focus 95

A-1 System software design 100

B-1 Dimensions of Head 2 x-ray source 103

List of Tables

4.1 Details of the IBM SP nodes at MIT 49

Chapter 1

Introduction to Zone-Plate-Array Lithography (ZPAL)

Zone-Plate-Array Lithography (ZPAL) is a direct-write technique using an array of zone plates to transfer patterns onto a substrate. This novel method of lithography combines the economic advantages of a maskless scheme and the high throughput of a massively parallel system as well. In this chapter, we first describe a working ZPAL system. Then, we go on to provide some background information on this project and finally demonstrate the need for a simulation study.

Chapter 2 describes the geometrical construction of zone plates. The necessary equations are developed and preliminary optical properties are discussed.

Chapter 3 treats the diffraction properties of zone plates in a detailed manner. Fresnel-Huygens principle is introduced as the first practical theory of diffraction. We also derive the Fresnel-Kirchhoff diffraction formula.

Chapter 4 introduces the relevant numerical techniques and discusses the issues involved.

Chapter 5 includes simulation studies of zone plate design and geometry. The effect of the source and zone-plate parameters on lithographic figures-of-merit are discussed. Pattern simulation results are shown and compared to the experimental results.

Chapter 6 examines the theory and simulations for an improved x-ray source

design. The brightness of the old and the proposed designs are compared.

Chapter 7 wraps up the thesis with the summary and recommendations for future work.

1.1 System Description

The ZPAL system consists of 4 main parts: the substrate, the array of zone plates, the spatial light modulators (SLMs) and the source of radiation. The substrate can be, for example, a silicon wafer mounted on an X-Y stage. It is coated with photoresist, which is sensitive to the patterning radiation. The zone plates behave like small lenses and focus the radiation into an array of spots on the wafer. Planar techniques are used to fabricate these zone plates. X-ray zone plates are typically fabricated on membranes and UV zone plates on glass substrates. In ZPAL, the spatial light modulators control the radiation incident on each zone plate. These SLMs can be either reflective (micromirrors) or transmissive (in-line shutters). Software control enables them to act as a *dynamic mask*, when viewed in the context of the whole system. The source of radiation is either a laser, a bright lamp with appropriate filters, or any other source with good spatial coherence. The main concern with regard to the source is the temporal and spatial coherence of the radiation. An illustration of the ZPAL system is shown in Figure 1-1. The SLM shown in the schematic is an array of transmissive in-line shutters.

Each zone plate is responsible for writing the pixels in the region of the substrate underneath it. This region is defined as the zone-plate unit cell. Since every zone plate writes different portions of the substrate simultaneously, the whole pattern is written in a massively parallel fashion. While the substrate is raster-scanned[1] on the stage, each zone plate focuses the light into a spot on the pixel underneath it at that instant in time. One zone plate is, in turn, addressed by one SLM, which controls how much light is incident on the zone plate and hence gets focussed onto the substrate. Thus, the SLM behaves as a dynamic mask.

[1]Note that the zone plates can be staggered and the substrate linearly scanned

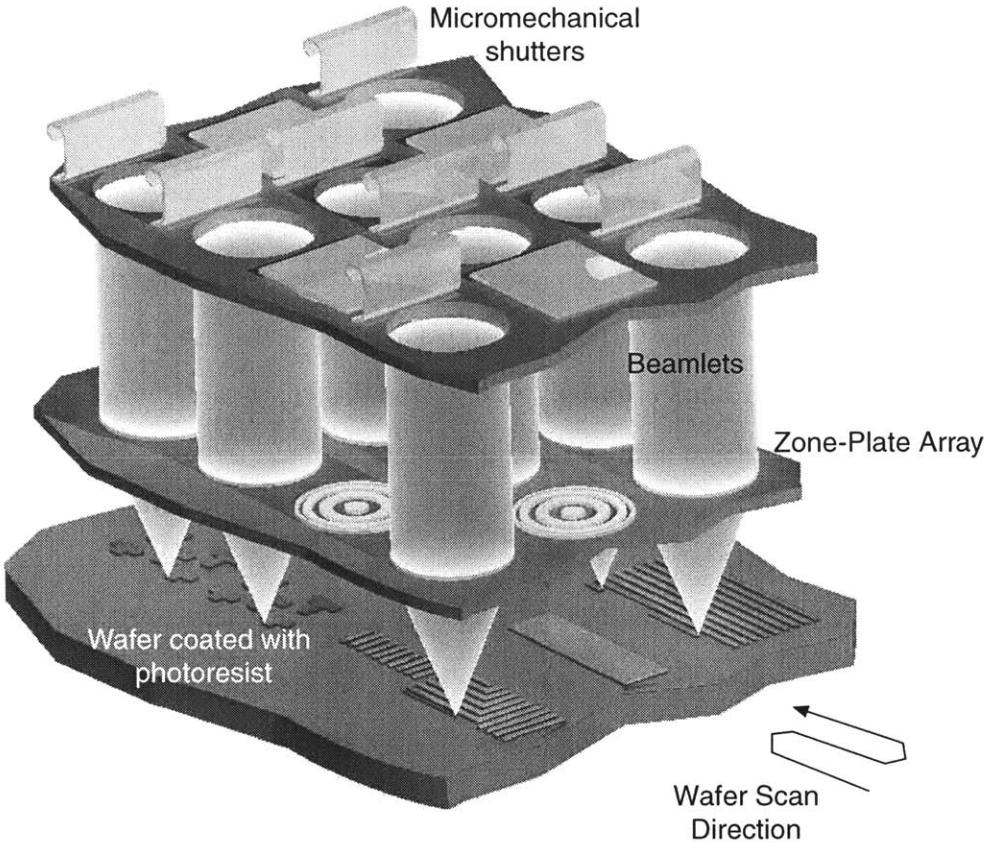

Figure 1-1: A ZPAL system.

1.2 Development of the Project

The basic idea for ZPAL was proposed by Smith[1]. A system design based on 25 nm lithographic resolution at $\lambda = 4.5$ nm was put forward. Using a microundulator designed for a synchrotron source and PMMA resist, a throughput of 1 cm^2/s was calculated. Preliminary work on ZPAL[2, 3] showed patterns written on thick resist using 193 nm ArF laser but without using any SLMs. Preliminary system design and simulations were also presented[4]. Recent studies[5, 6, 7] showed the feasibility of parallel patterning by ZPAL in the UV regime. The SLMs used in this case were the Texas Instruments Micromirror Array, and arbitrary patterns were written in resist. The minimum feature size written was 350 nm at an exposing wavelength of 442 nm. These recent studies cover some of the work detailed in this thesis. An overview of

lithography research in the NanoStructures laboratory at MIT is given in [8].

1.3 Motivation for Simulations

In lithography, the figures-of-merit are well defined. We need to get the smallest minimum feature size, with the highest pattern contrast and fidelity. We also need a reasonable gap between the lens (zone plate) and the substrate, with a large depth-of-focus. These goals are affected by not only the design of the zone plates themselves, but also by the radiation source and the geometry of the system. And many of these effects are not explicit or obvious. This necessitates numerical simulation tools, which could be used to study, understand and hence utilize these effects in an optimized design for the ZPAL system. The tools would have to simulate the diffraction of the light by the zone plates, taking into account all the system parameters of the source, the zone plate and the working distances. With a knowledge of the diffracted light, we would be able to simulate patterns on the resist-coated substrate, and hence carefully analyze the above-mentioned figures-of-merit. An overview of the inputs and outputs of the simulation tools is presented in Figure 1-2.

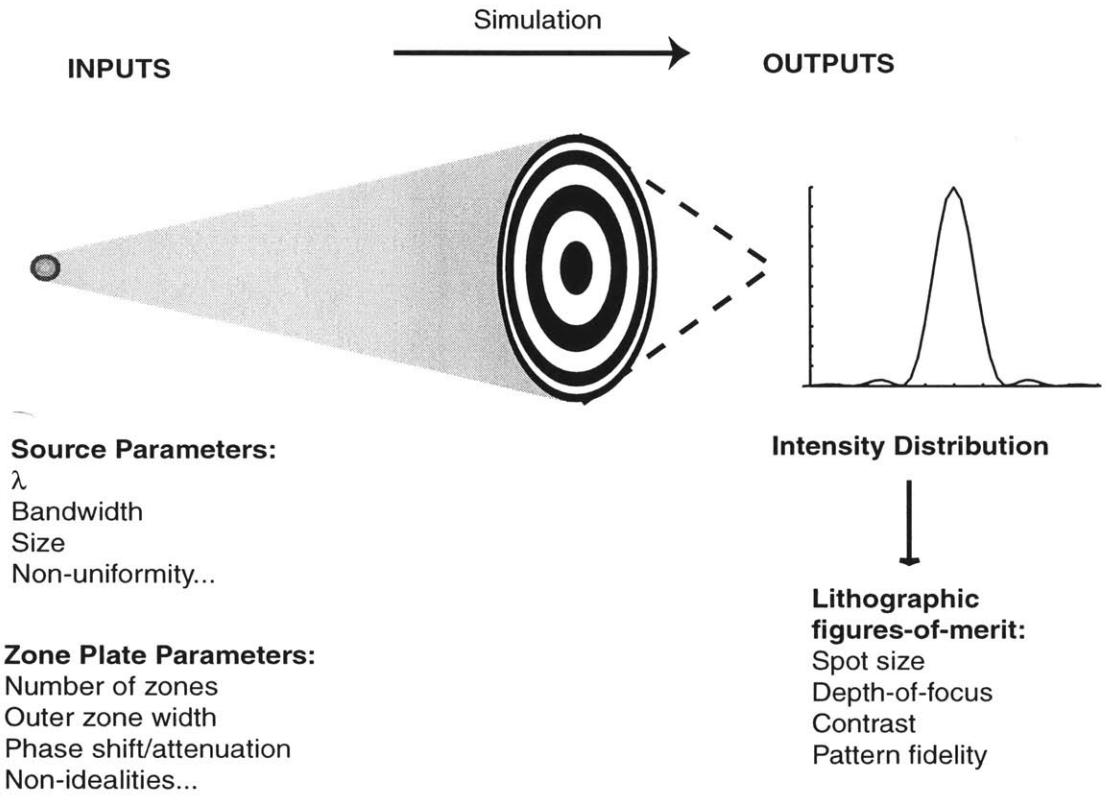

Figure 1-2: Overview of Simulations

Chapter 2

Optical Properties of Zone Plates

Zone plates, as focusing diffractive optical elements, were first proposed by Lord Rayleigh [9] and independently by Soret [10] about 120 years ago. The understanding and application of diffractive optics has come a long way since then. In recent decades, the effort has been to extend the capabilities to shorter wavelengths in the electromagnetic spectrum, where refractive lenses are either unavailable or extremely expensive. Among other applications, the zone plate has been used for coded imaging of x-ray and gamma-ray sources, for extensive holographic applications, for building atom interferometers and, more recently, for lithography. In this chapter, we discuss the geometry of the zone plate, which leads us to an understanding of its optical properties.

2.1 Geometry and Optics

The simplest form of a zone plate consists of a set of concentric circles whose radii are proportional to the square root of the natural numbers. The spaces between alternate rings are made opaque to the radiation. This object is capable of bringing to focus a parallel beam of light, much like a conventional refractive convex lens. This can be understood by appealing to Huygen's Principle. The dark regions on the zone plate block the disturbances from the alternate Huygen's zones on the wave-front. The zones are so constructed that the transparent zones ensure a constructive interference

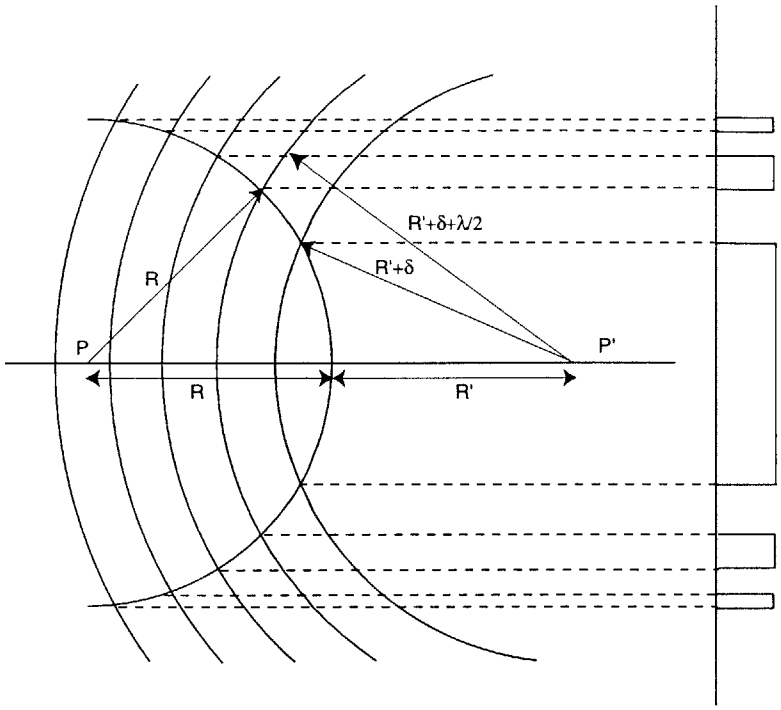

Figure 2-1: Construction of a Zone Plate.

at the focal spot.

The zone plate can also be visualized as a hologram formed by two point sources [11]. The wavefront from P (see Figure 2-1) may be imagined to be divided into a set of half-wavelength zones by spherical wavefronts differing in radii by $\lambda/2$ and having P' as the center. As seen from P', the adjacent zones will then transmit light of opposite phase. Hence, if the alternate zones are blocked out, then the transmitted zones all have the same phase and will constructively interfere at P'. If these zones are projected onto a plane perpendicular to the line joining P and P', we can construct a zone plate. All such zones approximately have equal areas (except for the first zone, which depends on the initial phase). The zone plate can also be considered as a hologram formed by a uniform plane wave and a spherical wave. When alternate zones are made opaque, it is called a Fresnel or an amplitude zone plate. Figure 2-2 shows such a zone plate. A positive zone plate is one with a transparent center as opposed to a negative zone plate whose center is opaque.

In Figure 2-3, we see a plane wave incident on a zone plate and focussed to a point, as expected of a lens. With the notations shown in the figure, we can derive

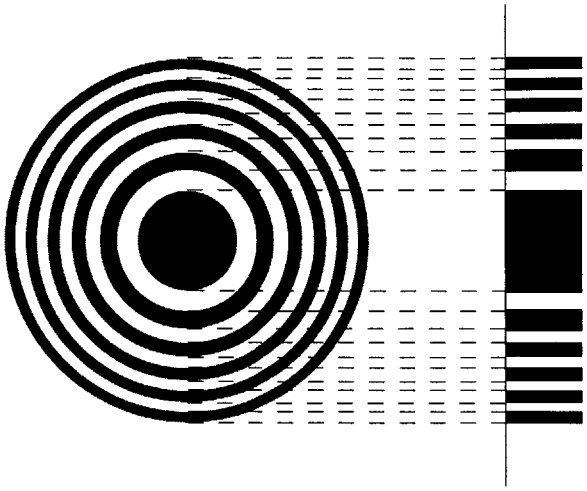

Figure 2-2: A Zone Plate.

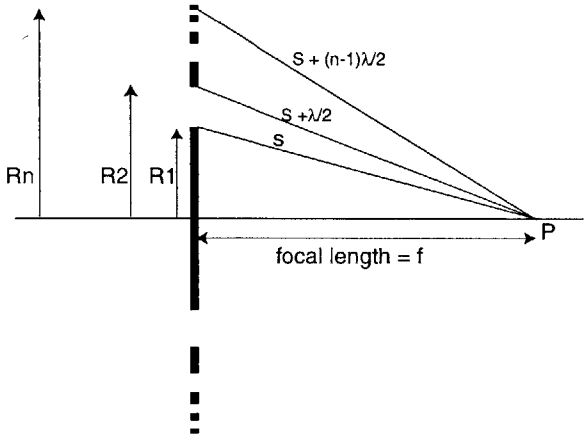

Figure 2-3: Derivation of expressions for zone radii.

the basic expressions for the zone radii.

$$R_1^2 + f^2 = S^2 \tag{2.1}$$

$$R_n^2 + f^2 = (S + \frac{(n-1)\lambda}{2})^2$$

$$\Rightarrow R_n^2 = R_1^2 + (n-1)\lambda\sqrt{f^2 + R_1^2} + \frac{(n-1)^2\lambda^2}{4} \tag{2.2}$$

Now, if we design the zone plate to have an outer-zone width, OZW and number

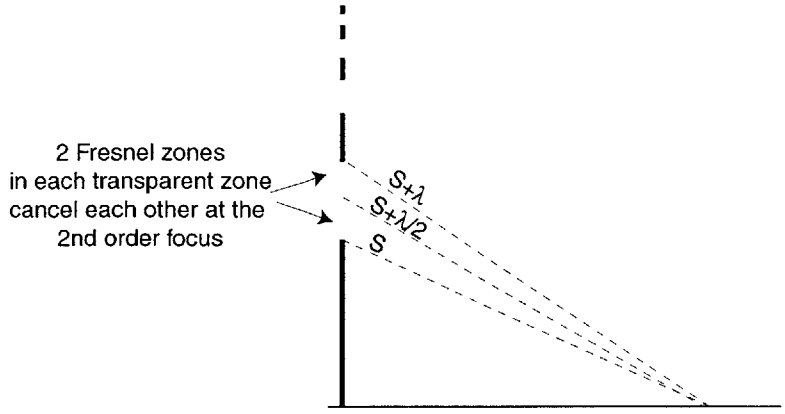

Figure 2-4: The transparent region has 2 Fresnel zones, which cancel each other at the 2nd order focus. This is true for all even orders.

of zones, N, we can write,

$$OZW = \sqrt{R_1^2 + (N-1)\lambda\sqrt{f^2 + R_1^2} + \frac{(N-1)^2\lambda^2}{4}} - \sqrt{R_1^2 + (N-2)\lambda\sqrt{f^2 + R_1^2} + \frac{(N-2)^2\lambda^2}{4}} \tag{2.3}$$

It must also be noted that the zone construction technique described in Figure 2-3 can be extended to higher orders of diffraction. This is done by choosing $mn\lambda/2$ as the optical path length difference between the n^{th} and the $(n-1)^{th}$ zones, where m is the order of the diffracted radiation ($= \pm 2, \pm 3, ...$). There are m Fresnel zones in each transparent (and opaque) region of the zone plate. Hence, if m is even, we can see that the light from these Fresnel zones cancel out and there are no even order foci. This is illustrated for the 2nd order in Figure 2-4.

In general for the m^{th} order focal length of f_m,

$$\begin{aligned} R_1^2 + f_m^2 &= S^2 \\ R_n^2 + f_m^2 &= (S + \frac{m(n-1)\lambda}{2})^2 \\ \Rightarrow R_n^2 &= R_1^2 + m(n-1)\lambda\sqrt{f_m^2 + R_1^2} + \frac{m^2(n-1)^2\lambda^2}{4} \end{aligned} \tag{2.4}$$

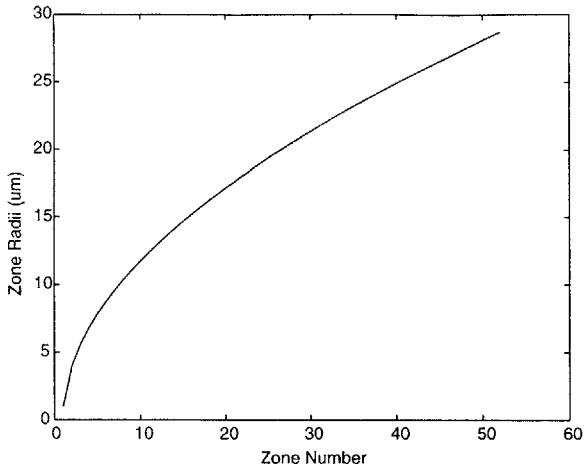

Figure 2-5: Radii of the zones for a zone plate with $f = 50\,\mu m, N = 52, OZW = 300\,nm, \lambda = 300\,nm$.

$$OZW = \sqrt{R_1^2 + m(N-1)\lambda\sqrt{f_m^2 + R_1^2} + \frac{m^2(N-1)^2\lambda^2}{4}} - \sqrt{R_1^2 + m(N-2)\lambda\sqrt{f_m^2 + R_1^2} + \frac{m^2(N-2)^2\lambda^2}{4}} \tag{2.5}$$

Using the Equations 2.4 and 2.5, we can numerically design a zone plate for any arbitrary order focus.

Zone plate design for the first order is based on the set of Equations 2.2 and 2.3. We can define the entire geometry of a zone plate in terms of the 4 parameters: f, OZW, N, and λ. The equations can be solved numerically in Matlab and the solution consists of the zone plate radii. These can also be used in zone plate fabrication by electron-beam lithography [12, 13, 14]. A typical plot of the calculated zone radii for a particular zone plate design is shown in Figure 2-5. As expected, the radii show an approximate quadratic relation to the zone-number.

An interesting point is that not all values of the inputs give rise to a real zone plate. This is illustrated by a 2-dimensional phase plot in Figure 2-6. Every point on this plot is a zone plate with a different λ and N (OZW and f are kept fixed). The black regions of the plot indicate the input values where zone plates are possible. The jagged edges are due to the quantization of λ.

Here we introduce the important concept of numerical aperture (NA). The NA of

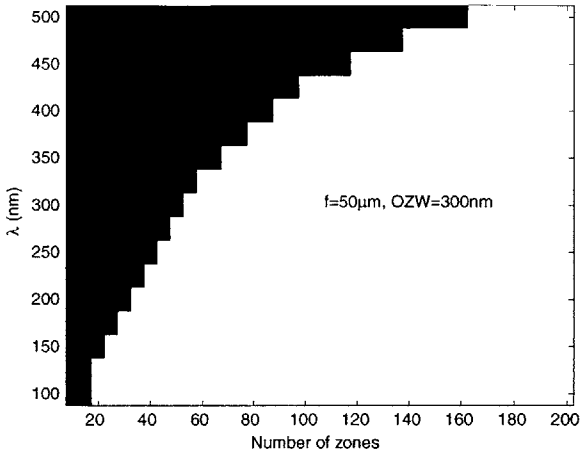

Figure 2-6: Dark regions show possible zone plate designs for $f = 50\,\mu m, OZW = 300\,nm$, and different combinations of λ and N. White regions are those where zone plate designs are not possible.

a lens is defined as

$$NA \equiv sin\,\theta,$$

where θ is the half angle measured from the focus to the lens. A higher NA lens corresponds to a larger angle of convergence. For a zone plate, we can write:

$$NA = \frac{R_N}{\sqrt{R_N^2 + f^2}}, \tag{2.6}$$

where R_N and f are the radius and the focal length of the zone plate respectively.

An analysis of the higher order foci of zone plates shows some interesting features. We show here that for very high-NA zone plates, only one focus exists in the strict sense. In other words, there is only one point on the optical axis of a high NA zone plate, where light diffracted from all open zones constructively interfere. We can look at the difference in the optical path lengths between adjacent zones to any point on the axis. Only when this difference is an integer multiple of $\lambda/2$ will light from alternate zones constructively interfere. In the calculations below, we first express the path difference between adjacent zones in terms of $\lambda/2$ and then we examine its fractional part. This fraction is a measure of how far a point is from becoming a

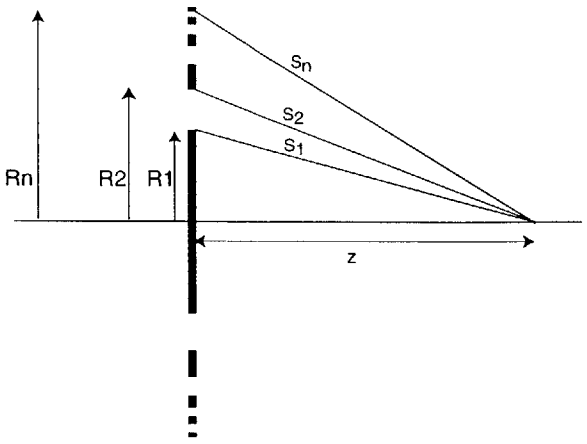

Figure 2-7: Optical path lengths from all zones to a point on the axis.

focus. Referring to Figure 2-7,

$$S_1 = \sqrt{R_1^2 + z^2}$$
$$S_2 = \sqrt{R_2^2 + z^2}$$
$$S_n = \sqrt{R_n^2 + z^2}$$

$$\phi_1 = \frac{S_2 - S_1}{\lambda/2}$$
$$\phi_2 = \frac{S_3 - S_2}{\lambda/2}$$
$$\phi_{n-1} = \frac{S_n - S_{n-1}}{\lambda/2}$$

$$Error = \sum_{i=1}^{N-1} \{\phi_i\}^2, \tag{2.7}$$
$$\text{where} \{\phi\} = \phi - int[\phi],$$

and $int[x]$ is the value, when x is rounded to the nearest integer. $Error$ is a measure of the deviation of ϕ from an integer for all the zones. This in turn represents, for any point on the axis, how far it is from having constructive interference. We plot an

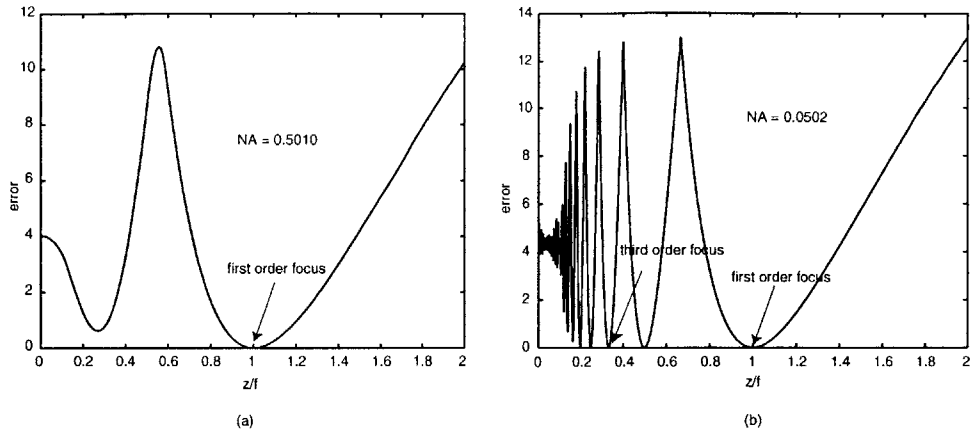

Figure 2-8: Plot showing deviation from constructive interference for all zones versus distance along the optical axis, normalized to the focal length. For (a), OZW = 300 nm, $f = 50\,\mu m$, λ = 300 nm and $N = 50$ ($NA = 0.5$). For (b), OZW = 45 nm, $f = 100\,\mu m$, λ = 4.5 nm and $N = 53$ ($NA = 0.05$).

example calculation of *error* versus z/f for two zone plates. *Figure* 2-8(a) shows a zone plate with OZW = 300 nm, $f = 50\,\mu m$, λ = 300 nm and $N = 50$ ($NA = 0.5$). Quite evidently, at $z = f$, the designed focus, we see the *error* go to 0. More importantly, at every other point on the axis, we notice that the *error* never goes to 0. On the other hand, in *Figure* 2-8(b), we show the same plot for a zone plate with OZW = 45 nm, $f = 100\,\mu m$, λ = 4.5 nm and $N = 53$ ($NA = 0.05$). Here we can clearly see a few higher orders. The even orders also show up as a zero in the error as defined in Equation 2.7, however as explained earlier, they do not form foci. This is an important understanding for ZPAL, since almost all the zone plates, fabricated to demonstrate ZPAL have been of high NA.

Classically, people have studied the geometry of the zone plates using certain approximations to obtain simple, analytical expressions. In Equation 2.1, the path length of the first zone to the focus is set to $f + \lambda/2$. This leads to the following

simplified expression.

$$R_1^2 = \lambda f + \frac{\lambda^2}{4}$$

$$\Rightarrow R_n^2 = n\lambda f + \frac{n^2\lambda^2}{4} \tag{2.8}$$

$$\Rightarrow f = \frac{(4OZW^2 - \lambda^2)(2N-1) + 2\sqrt{4N(N-1)OZW^2(4OZW^2 - \lambda^2)}}{4\lambda} \tag{2.9}$$

The interesting point here is that by setting the initial phase, we essentially fix one degree of freedom, usually the focal length. This means that now only 3 parameters are necessary to fix a zone plate.

In many cases, the second term in Equation 2.8 is much smaller than the the first, then

$$R_n^2 \approx n\lambda f. \tag{2.10}$$

In order to have a sense of the errors involved, we can compare the zone radii computed using the exact Equations 2.2 and 2.3 to those computed using the Equation 2.10. We can plot the difference in the zone radii as computed by the two methods as a function of the zone number. This is shown in Figure 2-9 along with the exact zone radii for comparison. This computation was performed for a zone plate with $f = 50\,\mu m, N = 52, OZW = 300\,nm, \lambda = 300\,nm$. Equation 2.10 implies that R_n^2 is periodic in the zone number. If the number of zones is large, then we can conceptually think about an *infinite* zone plate, which will diffract any incident light into many different orders, very similar to an infinite grating. This can be analyzed by expanding the transmission function of the zone plate as a Fourier series in R^2 [15, 16].

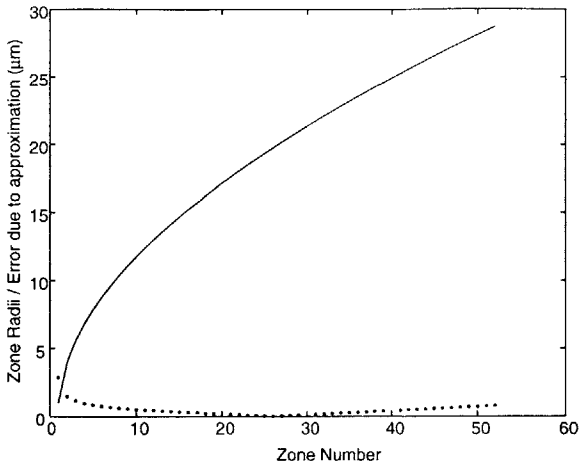

Figure 2-9: Zone radii plotted versus the number of zones for a zone plate with $f = 50\,\mu m, N = 52, OZW = 300\,nm, \lambda = 300\,nm$. The dotted line shows the absolute deviation of the radii computed by Equation 2.10 from the exact values.

$$f(R^2) = \sum_{m=-\infty}^{\infty} c_m cos(mR^2) \tag{2.11}$$

$$c_m = \frac{1}{2\pi}\int_{-\pi}^{\pi} f(R^2)d(R^2)$$

$$c_m = \frac{1}{\pi}\int_{0}^{\pi/2} cos(mu)du$$

$$\Rightarrow c_m = \frac{sin(m\pi/2)}{m\pi} \tag{2.12}$$

Since the diffraction efficiencies to the various orders $\propto c_m^2$, we can calculate efficiency of the m^{th} order, η_m,

$$\eta_m = \begin{cases} \frac{1}{4} & m = 0 \\ \frac{1}{m^2\pi^2} & m\,odd \\ 0 & m\,even \end{cases} \tag{2.13}$$

Thus half the incident energy is absorbed by the zone plate. In order to improve the efficiency, Lord Rayleigh first suggested the use of phase-reversing alternate zones [9]. This phase zone plate makes use of the fact that the field from adjacent zones constructively interfere and hence the efficiency is increased by a factor of 4. The

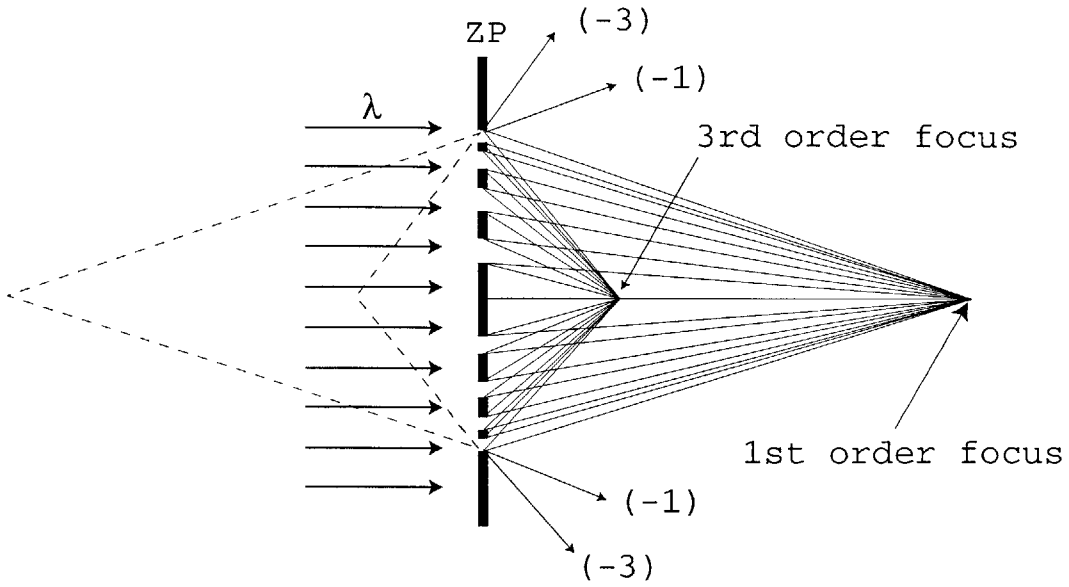

Figure 2-10: Zone plate showing ± 1 and ± 3 order radiation.

different orders as focussed by a zone plate are shown in Figure 2-10. In the next chapter, the diffraction properties of zone plates are studied.

Chapter 3

Diffraction by Zone Plates

In this chapter, we analyze the properties of light diffracted by a zone plate, especially the point-spread function. We derive the expressions for the scalar theory of diffraction. With the Fresnel-Kirchoff approximation, these integrals are numerically evaluated to describe the diffracted fields. Finally, we discuss the effects of various zone-plate design parameters on the lithographic figures-of-merit.

3.1 Huygens-Fresnel Principle

When light encounters an obstacle, opaque or transparent, its propagation deviates from that predicted by the theory of geometrical optics (that light travels in straight lines). This phenomenon is a result of the wave nature of light and is termed diffraction. Huygens' principle [16, 17], the first physical theory to qualitatively explain diffraction involves the following statements: 1) Every point on a wavefront of light can be considered as a source for a secondary disturbance which produces a spherical wavelet; 2) The position of the wavefront at any later time is the envelope of such wavelets; 3) The frequency and speed of the wavelets is the same as that of the primary waves.

In order to describe the amplitude distribution on a wavefront, Fresnel introduced the concept of interference into the Huygens' principle [16, 18]. He postulated that the amplitude at any point in the future is a superposition of the wavelets.

According to the Huygens-Fresnel principle, the field at any point in the plane of observation can be derived as an integration of the contributions from all the wavelets coming from the aperture. Consider an infinitesimal area dS at a point P_1 in an aperture S (see Figure 3-1). The contribution of a wavelet from point P_1 at a point P_2 is given by

$$U(P_1)\frac{exp(-ikr)}{r}dS, \tag{3.1}$$

where $U(P_1)$ is the field amplitude at P_1 due to the light incident from the left.

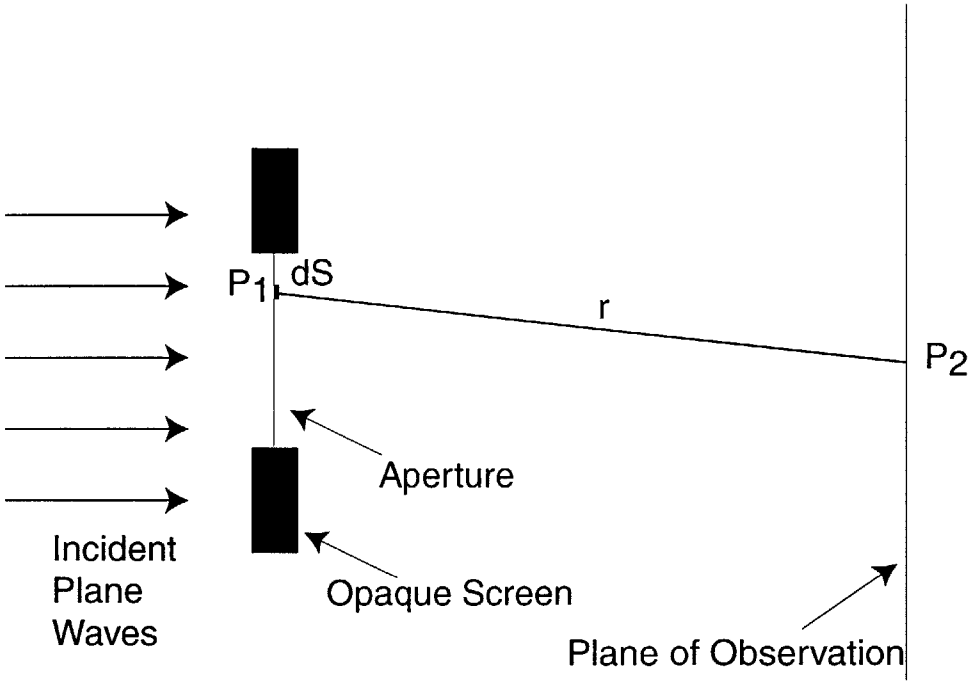

Figure 3-1: Derivation of the mathematical expression for Fresnel-Huygens Principle.

Hence, the total field at P_2 due to the incident field being diffracted by the aperture is given by

$$U(P_2) = C\iint_S \frac{exp(-ikr)}{r}U(P_1)\,dS, \tag{3.2}$$

where C is a constant and the integral is over the area of the aperture. Using this mathematical expression of the Huygens-Fresnel principle, we can calculate the

diffraction patterns of arbitrary apertures. Consider the case of a small aperture, illuminated by uniform plane waves. We notice that the diffraction pattern in the plane of observation depends on the distance (d) of the observation plane from the aperture. These patterns can be qualitatively divided into 3 types.

1) When d is very small, the pattern is essentially a projection of the aperture with fringing effects at the aperture boundaries. This is the near-field region.

2) When d is intermediate, the fringes are more pronounced, and the structure of the pattern changes with d. This is the Fresnel diffraction region.

3) When d is very large, the structure of the pattern does not change with d but its size does. This is called the Fraunhofer or the far-field diffraction region. A practical rule of thumb to demarcate this region is

$$d > \frac{a^2}{\lambda}, \tag{3.3}$$

where a is the greatest width of the aperture and λ is the wavelength of the illuminating radiation. Figure 3-2 shows the 3 regions of diffraction.

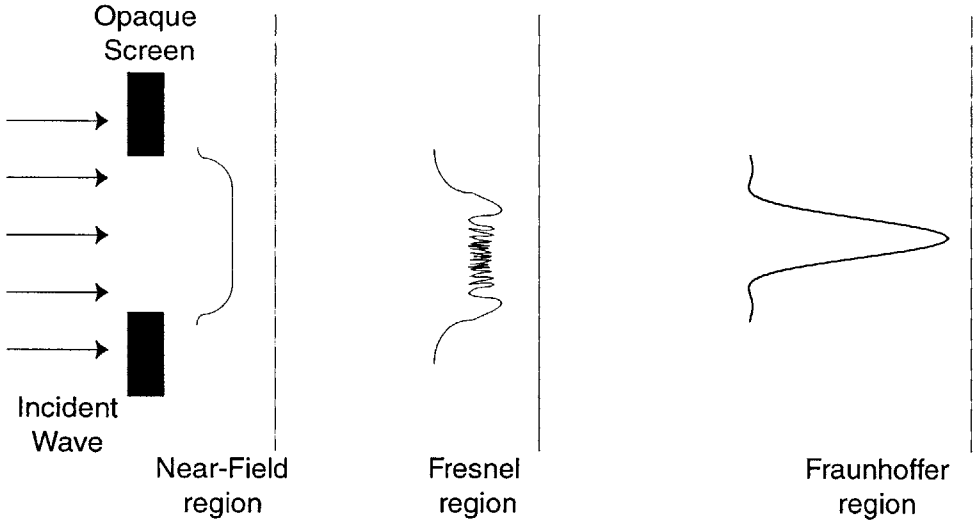

Figure 3-2: Illustration of the 3 different regions of diffraction.

3.2 Fresnel-Kirchhoff Diffraction Theory

A rigorous theory for diffraction can be derived from Maxwell's equations. Here, we consider the scalar form of the equations.

A time-harmonic beam of light at point P and time t can be represented as

$$\phi(P,t) = Re\{U(P)\, exp(i2\pi\, f_\nu\, t + i\theta(P))\}, \tag{3.4}$$

where f_ν is the frequency of the light and $\theta(P)$ is the phase at point P. Using Maxwell's equations [17], we can derive the Helmholtz wave equation.

$$\begin{aligned} &(\nabla^2 + k^2)\, U(P) = 0, \\ &\text{where } \nabla^2 = \frac{\partial^2}{\partial x^2} + \frac{\partial^2}{\partial y^2} + \frac{\partial^2}{\partial z^2}, \\ &\text{and } k = \frac{2\pi}{\lambda}. \end{aligned} \tag{3.5}$$

For two solutions U and U' to Equation 3.5, Green's theorem [17, 16] stipulates that

$$\iint_S (U' \frac{\partial U}{\partial n} - U \frac{\partial U'}{\partial n})\, dS = 0, \tag{3.6}$$

where S is a closed surface and $\boldsymbol{n}$ is the unit vector of the normal to the surface pointing into the enclosed volume. This also requires that U and U' have continuous first and second order derivatives on and inside the surface S. Hence, by choosing an appropriate Green's function for U', we can derive an expression for U at any point inside the surface S.

Kirchhoff assumed a Green's function of the form

$$U'(P_1) = \frac{exp(-ikr)}{r}, \tag{3.7}$$

which represents a spherical wave originating from P and observed at a point P_1. The distance between P and P_1 is r. This function is a solution to Equation 3.5, except

at its singularity, when $r = 0$. Now if we cover the singularity by a spherical surface, S' of infinitesimal radius ϵ (Figure 3-3), the closed surface in Equation 3.6 can be represented by two surfaces S and S'. This leads to

$$\iint_S (U'\frac{\partial U}{\partial n} - U\frac{\partial U'}{\partial n})\, dS = -\iint_{S'} (U'\frac{\partial U}{\partial n} - U\frac{\partial U'}{\partial n})\, dS.$$

Using Equation 3.7 for a point P_1 on the surface S' and taking the limit $\epsilon \longrightarrow 0$,

$$\iint_{S'} (U'\frac{\partial U}{\partial n} - U\frac{\partial U'}{\partial n})\, dS = -4\pi U(P).$$

Equation 3.7 $\Rightarrow$

$$U(P) = \frac{1}{4\pi} \iint_S [U\frac{\partial}{\partial n}(\frac{exp(-ikr)}{r}) - \frac{exp(-ikr)}{r}\frac{\partial U}{\partial n}]\, dS. \tag{3.8}$$

Equation 3.8 is a rigorous solution of the Helmholtz equation and is known as the Kirchhoff diffraction integral.

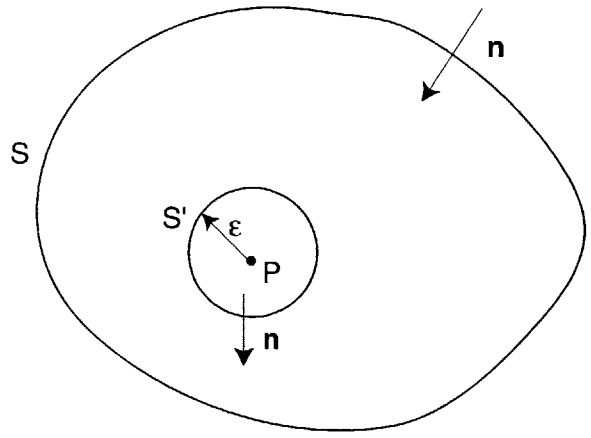

Figure 3-3: Two closed surfaces around a point P where a spherical wavelet has a singularity.

Now, let us consider a plane opaque screen with an aperture Σ as shown in Figure 3-4. If we are interested in calculating the field contribution at a point P due to a point source at S_0, we have to use Equation 3.8 with $S = \Sigma + S_1 + S_2$. As shown in Figure 3-4, S_1 is the area of the screen opaque to light and S_2 is a large surface, such that P is enclosed by S. In order to evaluate Equation 3.8, Kirchhoff made the

following assumptions for the boundary conditions of the field and its derivative:

1) The field within Σ is the same as when the screen is not present.

2) In the opaque area of the screen, i.e., on S_1, $U = 0$ and $\frac{\partial U}{\partial n} = 0$.

These are known as the Kirchhoff boundary conditions.

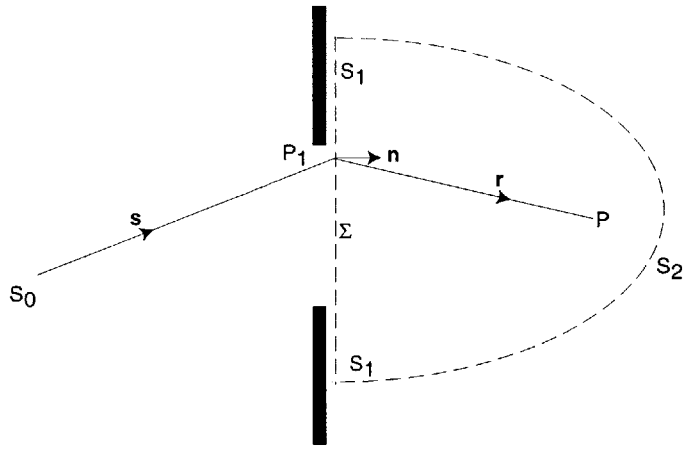

Figure 3-4: Diffraction by an arbitrary aperture.

The integral in Equation 3.8 should be evaluated over the 3 surfaces. The integral over S_2 can be shown to be 0 by making the surface very large such that for all time, light traveling at a finite velocity never reaches it. By virtue of the 2nd Kirchhoff boundary condition, the integral over S_1 is also 0. Now for the integral over the aperture, Σ, let us concentrate on a point P_1 on Σ. The 1st Kirchhoff boundary condition implies that

$$U(P_1) = U_0 \frac{exp(-iks)}{s} \tag{3.9}$$

$$\Rightarrow \frac{\partial U}{\partial n} = U_0 \frac{exp(-iks)}{s}(-ik - \frac{1}{s})cos(\boldsymbol{n}, \boldsymbol{s}) \approx -U_0 \frac{ik}{s} exp(-iks)cos(\boldsymbol{n}, \boldsymbol{s}), \tag{3.10}$$

$$\frac{\partial}{\partial n}(\frac{exp(-ikr)}{r}) = \frac{exp(-ikr)}{r}(-ik - \frac{1}{r})cos(\boldsymbol{n}, \boldsymbol{r}) \approx -\frac{ik}{r} exp(-ikr)cos(\boldsymbol{n}, \boldsymbol{r}), \tag{3.11}$$

And Equation 3.8 implies

$$U(P) = \frac{iU_0}{\lambda} \iint_{\Sigma} \frac{exp(-ik(r+s))}{rs} \frac{cos(\boldsymbol{n}, \boldsymbol{s}) - cos(\boldsymbol{n}, \boldsymbol{r})}{2} dS \tag{3.12}$$

Equation 3.12 is known as the Fresnel-Kirchhoff diffraction formula. The approximations in Equations 3.10 and 3.11 are true when $s >> \lambda$ and $r >> \lambda$ respectively. It must be pointed out here that the Kirchhoff boundary conditions are mathematically inconsistent, as is evident from the following two observations. Firstly, the 2nd boundary condition implies that the solution to the wave equation is actually 0 everywhere. Secondly, the Equation 3.12 does not reproduce the Kirchhoff boundary conditions. Despite these weaknesses, this is very widely used in practice because of remarkable agreement with observed results [17].

In order to study the various lithographic figures-of-merit for ZPAL, one needs to analyze the 3-dimensional field distribution at the focal point of a zone plate. We follow the conventional point-spread function analysis here. In the next section, we look at approximate but explicit expressions for the point-spread function. Then we go on to numerically evaluate the exact Fresnel-Kirchhoff diffraction equation for a zone plate.

3.3 Point-Spread Function Analysis for a Zone Plate

The approach followed here is to numerically evaluate the Fresnel-Kirchhoff diffraction integral with the zone plate as an aperture. This is illustrated in the Figure 3-5. In the case of an amplitude zone plate, the field at a point P_1, due to light from a point source at P, can be written as:

$$U(P_1, P) = \underbrace{\sum_{n=1}^{N-1}}_{\text{open zones}} \frac{iU_0}{\lambda} \int_{\rho=R_n}^{\rho=R_{n+1}} \int_{\theta=0}^{\theta=2\pi} \frac{exp(-ik(r+s))}{rs} \frac{cos(\boldsymbol{n},\boldsymbol{s}) - cos(\boldsymbol{n},\boldsymbol{r})}{2} \rho \, d\rho \, d\theta, \tag{3.13}$$

where (ρ, θ) is a point on the zone plate in cylindrical coordinates.

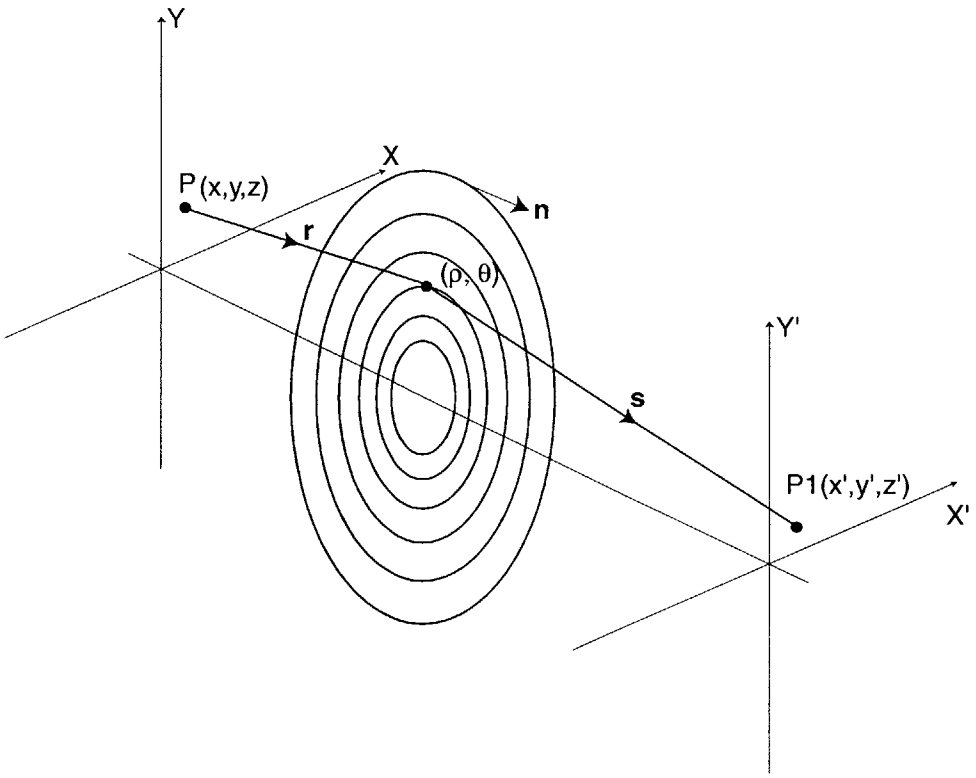

Figure 3-5: Fresnel-Kirchhoff diffraction for a zone plate.

For a phase zone plate, Equation 3.13 is modified as shown below:

$$U(P_1,P) = \underbrace{\sum_{n=1}^{N-1}}_{\text{all zones}} (-1)^{n+\mu}\frac{iU_0}{\lambda}\int_{\rho=R_n}^{\rho=R_{n+1}}\int_{\theta=0}^{\theta=2\pi}\frac{exp(-ik(r+s))}{rs}\frac{cos(\boldsymbol{n},\boldsymbol{s})-cos(\boldsymbol{n},\boldsymbol{r})}{2}\rho\,d\rho\,d\theta, \tag{3.14}$$

where $\mu = 0$, if the first zone has a π phase shift or else $\mu = 1$. If we consider sources that have radial symmetry, then the point spread function will also be radially symmetric.

In ZPAL, we are interested in the influence of the source parameters on the focused spot of a zone plate. Specifically, we would like to incorporate a source of finite size and a finite bandwidth into our diffraction calculations. This is especially important in our preliminary experiments for x-ray ZPAL, where we are using an electron bombardment x-ray source. We can analyze the contribution to a certain point P_1 from

every point on the source and we can assume that every such point on the source is temporally incoherent, i.e., has random phase. This is valid when the distance between the points considered is large compared to the wavelength of the photons emitted. Under these assumptions, we can add up intensity contributions from all such points on the source and this will give the total intensity at the observation point. The fact that photons of different wavelengths do not interfere with each other allows us to take into account the finite bandwidth of the source in a straightforward manner. The intensity contributions due to different wavelengths can be added up to give the total intensity distribution. Making the λ dependence of the field explicit, we can write from Equation 3.14,

$$I(P_1) = \iint_S \int_\lambda |U(P_1, P(x,y,z), \lambda)|^2 \, d\lambda \, dS \,, \tag{3.15}$$

where $I(P_1)$ is the intensity at point P_1, S is the cross-sectional area of the source illuminating the zone plate and the integral in λ is over the bandwidth of the source.

Chapter 4

Numerical Simulations

In this chapter, we first discuss the steps involved in computing the point-spread-function of a zone plate. Then, we validate our choice of a parallel processing model. We also review the advantages and limits of the available hardware and software at our disposal. A basic flow-chart of the entire computational process is shown in Figure 4-1.

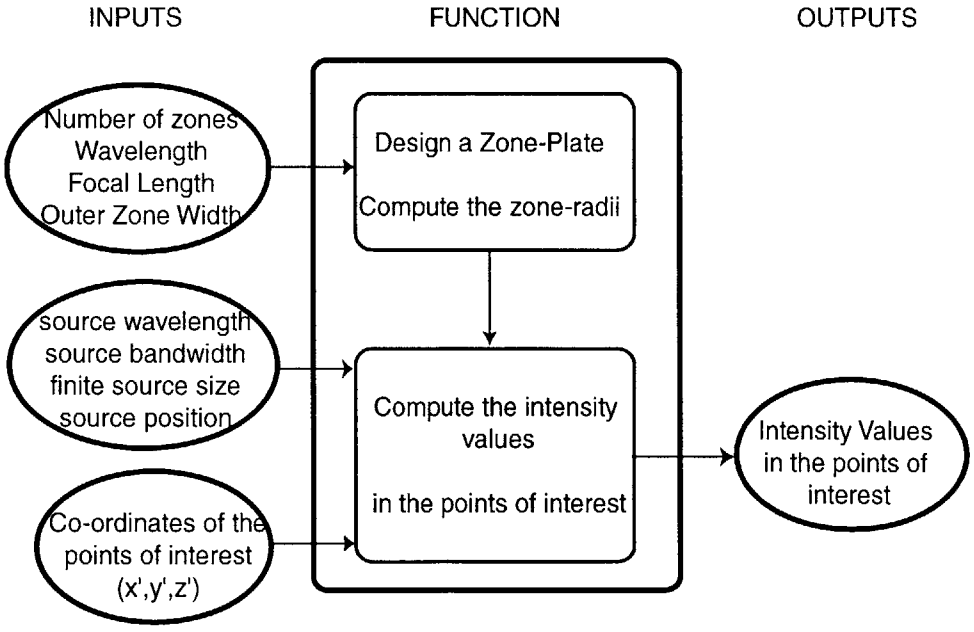

Figure 4-1: Basic flow chart of the simulations.

zone plate design is based on the set of Equations 2.2 and 2.3, and is discussed

in Chapter 2. It is obvious that most of the computational effort will be needed to evaluate the Fresnel-Kirchoff integral (Equation 3.12) at all the points in the region of interest. Since the field computed using Equation 3.12 at every point is independent of every other point, this computation is a good candidate for a parallel processing solution. We review some of the basic principles of parallel processing below.

4.1 Parallel Processing Concepts

Parallel processing is the execution of different parts of the same program by multiple processors simultaneously. The main purpose of this approach is to reduce the real execution time for numerical problems. Processing schemes can be classified into 4 categories based on how data and instruction streams interact [19]. This is illustrated in Figure 4-2.

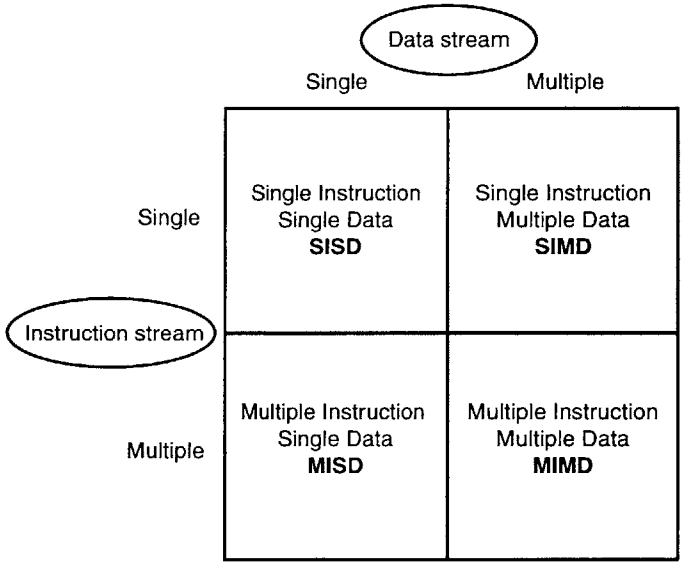

Figure 4-2: Categories of processing schemes.

Single Instruction Single Data (SISD) is the classical style of computing and is very prevalent in today's personal computers. During each clock cycle, the central processing unit (CPU) executes a single instruction stream acting upon a single data stream. Thus all instructions are executed in a serial manner.

Multiple Instruction Single Data (MISD) is the least common of all the categories. It is included here for the sake of completeness. Several different instruction streams act upon the same stream of data simultaneously. An example would be several cryptography algorithms trying to decode the same encoded message.

Single Instruction Multiple Data (SIMD) is perhaps the most important category with regard to parallel processing. In this case, the same instruction stream acts upon several different streams of data in parallel. A big problem is divided up into smaller pieces and the data relevant to each piece is delegated to one processor. All the processors perform the same task but on different pieces of data. Once the computation is carried out, all the processors return their respective outputs to the managing processor, which puts together the solution to all the pieces, to create a coherent whole.

Multiple Instruction Multiple Data (MIMD) is considered to be the next step in parallel computing, where many instruction streams can be applied simultaneously to multiple data streams. This is the most general of all the categories. However, the requirements for hardware and software are quite challenging.

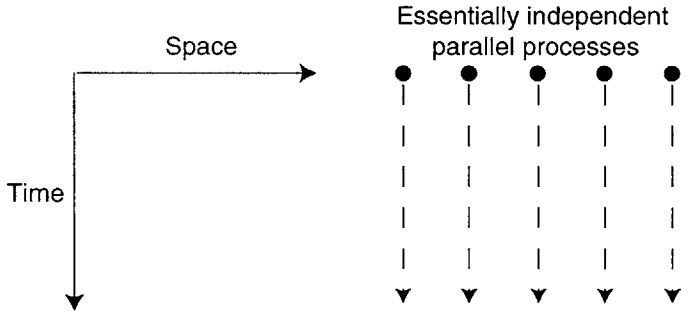

Figure 4-3: Parallelizing the problem. A large region of interest is divided among multiple processors and the fields at each point in space is independently calculated.

SIMD is the processing scheme most suited for our problem. The idea is to break up the big region of interest into many smaller sub-regions. Then each processor is responsible for calculating the field intensity in its sub-region. Finally, the field intensities from all the sub-regions are put together to obtain the field intensity in the entire region of interest. This is also called data parallelism, where each processor

does the same work on a unique piece of data. This is a highly scalable form of parallelism. In the scalar diffraction problem, the simple spatial structure leads to very clear parallelism. This problem belongs to a class of computational problems which are known as *embarrassingly parallel* [20]. The simple spatial structure of these problems imply that no complex temporal synchronization of the processors is required and the parallelization becomes straightforward (see Figure 4-3). One important feature of embarrassingly parallel problems is the modest node-to-node communications overhead. Although no spatial connection implies no inter-node communication, in a practical problem, some communication is necessary to set up the problem and accumulate the results. The low communication requirements of embarrassingly parallel problems make them suitable for implementation on distributed computing environments, such as the IBM SP, whose details are described below.

4.2 Details of Hardware

All the diffraction calculations were performed on the IBM SP at MIT. The RISC System/6000 Scalable POWERparallel System (SP) is a distributed memory machine from IBM. The system at MIT consists of 13 nodes (processor + memory), connected by an ethernet and a high speed switch. The nodes have POWER2 Super Chip (P2SC) architecture RS/6000 processors. These are superscalar pipelined chips capable of executing 4 floating point calculations per cycle [21]. The details of the nodes are shown in Table 4.1 [22]. The nodes communicate via HPS2 switch adapters. This machine was made possible by IBM's SUR program.

The plotting of figures and zone plate geometry calculations were performed in Matlab using a 450 MHz Pentium III desktop computer.

4.3 Details of Software

The operating system for the IBM SP is AIX 4.2.5, IBM's version of UNIX. It has Parallel Systems support program 2.3. The software for calculating the diffraction

Node	Memory(MB)	Clock-Speed(MHz)
1	512	133
2	512	133
3	512	133
4	512	133
5	256	133
6	256	133
7	256	133
8	256	133
9	256	133
10	256	133
11	256	133
12	256	133
13	1024	133

Table 4.1: Details of the IBM SP nodes at MIT

patterns was written in C language. In order to parallelize the code, we need to use certain library subroutines for task management and message passing. IBM provides the SP with the Message Passing Interface (MPI). MPI is a subroutine library for writing distributed memory parallel programs that conform to a vendor-independent standard and hence are reasonably portable. IBM's version of MPI has been optimized for performance on the SP architecture.

The design of the software first started with a debugged serial version of the program, written in C. Once we decided on the parallel algorithm as described earlier, the serial code was modified by incorporating the calls to the MPI library, specifically to distribute the tasks among the processors and manage the final computed results. This also sets the environment variables for the parallel processing programs. The most relevant environment variables are `MP_PROCS` and `MP_EUILIB`. `MP_PROCS` is the number of processors used in the program. `MP_EUILIB` determines the mode of communication by the nodes. It can be User Space (`US`), which uses the high-performance switch and enables the user to run the processes in a dedicated manner or it can be Internet Protocol (`IP`), which can use a slower ethernet connection. In embarrassingly parallel problems, the issue of communication overhead is usually not significant, so

the second variable is not a crucial choice. Detailed information on MPI functions and their usage can be found in the man pages (see also [19]).

The integrals necessary in the computation of the diffraction patterns are evaluated using subroutines provided by the IBM Parallel Engineering and Scientific Subroutine Library (Parallel ESSL). Parallel ESSL is a scalable mathematical subroutine library that supports parallel processing applications on the IBM SP. It supports the SIMD programming model and provides all major mathematical functions. The subroutines `DGLNQ` and `DGLNQ2` are used to perform the one-dimensional and two-dimensional numerical integrations respectively. These subroutines utilize the Gauss-Legendre quadrature method to evaluate the integrals. The details on how to use these subroutines can be found in the ESSL reference guide [23]. In the next section, we discuss the issues associated with the numerical integration.

4.4 Numerical Integration Issues

The integral of a one-dimensional function can be expressed as a sum of the function values at certain chosen points, weighted by corresponding weighting coefficients. This is known as the rule of Gaussian quadratures [24, 25].

$$\int_a^b w(x)\, f(x)\, dx \approx \sum_{j=1}^{N} W_j\, f(x_j), \tag{4.1}$$

where W_j are the weights and x_j are the corresponding sampling points and N is the order of the quadrature. In the particular case of a Gauss-Legendre quadrature, we have:

$$w(x) \equiv 1;\ -1 < x < 1 \tag{4.2}$$

$$W_j = \frac{2}{(1 - x_j^2)|P'_N(x_j)|^2} \tag{4.3}$$

$$P_N(x_j) = 0, \tag{4.4}$$

where P_j are the Legendre polynomials defined by the iterative relation:

$$(j+1)P_{j+1}(x) = (2j+1)xP_j(x) - jP_{j-1}(x);\ P_0(x) = 1,\ P_1(x) = x, \tag{4.5}$$

and

$$P'_N(x_j) = \left.\frac{dP_N(x)}{dx}\right|_{x=x_j} \tag{4.6}$$

Thus, the w_js are the zeros of the Legendre polynomial, $P_j(x)$. The W_js are calculated according to the Equations 4.2, 4.3, and 4.4. It can be shown that Equation 4.1 becomes exact, when the function $f(x)$ is of polynomial order $(2N-1)$ or less [25]. From Chapter 3, we know the Fresnel-Kirchhoff integral is:

$$U(P) = \frac{iU_0}{\lambda} \iint_{\Sigma} \frac{exp(-ik(r+s))}{rs} \frac{cos(\boldsymbol{n},\boldsymbol{s}) - cos(\boldsymbol{n},\boldsymbol{r})}{2}\, dS \tag{4.7}$$

The Gauss-Legendre quadrature method was used to compute this integral along the axis as well as in the transverse focal plane. It was more difficult to make the algorithm effective for points far off the optical axis due to the increased oscillatory nature of the phase factor in the integrand. Equation 4.7 can be written in terms of cylindrical coordinates:

$$U(P_1,P) = \int_{\rho=R_n}^{\rho=R_{n+1}} \int_{\theta=0}^{\theta=2\pi} \frac{iU_0}{\lambda} \frac{exp(-ik(r+s))}{rs} \frac{cos(\boldsymbol{n},\boldsymbol{s}) - cos(\boldsymbol{n},\boldsymbol{r})}{2}\, \rho\, d\rho\, d\theta, \tag{4.8}$$

It was observed that the maximum instability was present in the θ integral, especially for points of interest that were farthest from the optical axis of the zone plate. To overcome this problem, we divided the θ integration range of 0 to 2π into smaller integrals. The function is continuous in θ through those intervals. This dramatically improved the convergence of the numerical integration routines as illustrated in Figure 4-4. All three plots are for a zone plate with parameters $N = 76$, $f = 48\,\mu m$, $\lambda = 442\,nm$, and $OZW = 330\,nm$. The radius of this zone plate is about $50\,\mu m$.

The horizontal axis in all 3 plots is the order of the Gauss-Legendre quadrature of the θ integral. The lines with the circles show the intensity values using the above-mentioned sub-division method. The plain lines show the values using the normal algorithm. In (a), (b) and (c), the vertical axes are the intensity values of the field at radial distances of $10\,\mu m$, $50\,\mu m$ and $100\,\mu m$ from the axis, respectively. Also, note that the field at a smaller radial distance converges faster than one at a larger radial distance.

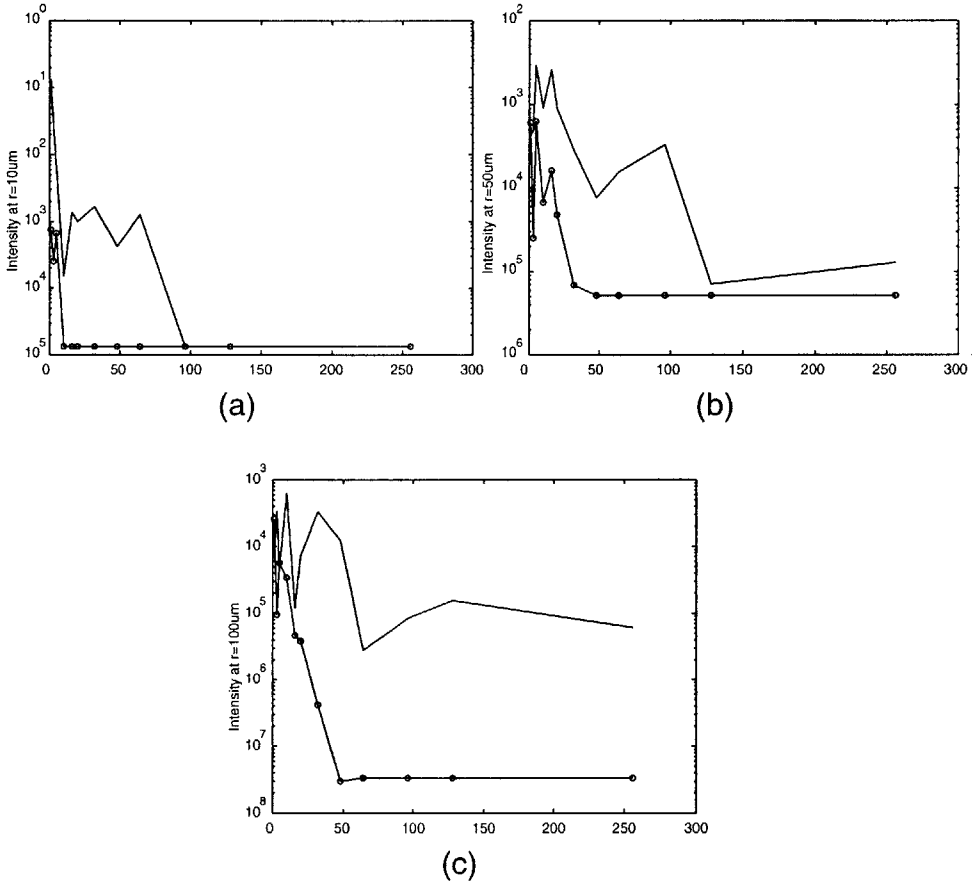

Figure 4-4: Study of convergence. All plots are for a zone plate with $N = 76$, $f = 48\,\mu m$, $\lambda = 442\,nm$, and $OZW = 330\,nm$. Intensity values at 3 different radial distances are plotted versus the order of the θ integral to show the improved convergence due to the subdivision of the θ range.

4.5 Timing Issues

Speedup is the ratio of the total serial execution time divided by the parallel execution time for the same problem size and number of processors. If speedup were perfect, it would equal the number of processors. Scalability is the ability of the problem to preserve the speedup as problem size and the number of processors are increased. As we mentioned earlier, the scalar diffraction problem is an embarrassingly parallel one. This implies that close to perfect speedup and scalability should be possible. The following plot shows the speedup attained versus the number of processors used. The problem was to compute the radial diffraction pattern at the focus of a zone plate with parameters: $\lambda = 442\,nm$, $OZW = 300\,nm$, $N = 76$ and $f = 50\,\mu m$. We can see that the speedup is almost equal to the number of processors used, as it must be for embarrassingly parallel problems. We can also see that for a larger number of processors, the curve starts to bend over, implying that the communication overheads start becoming important.

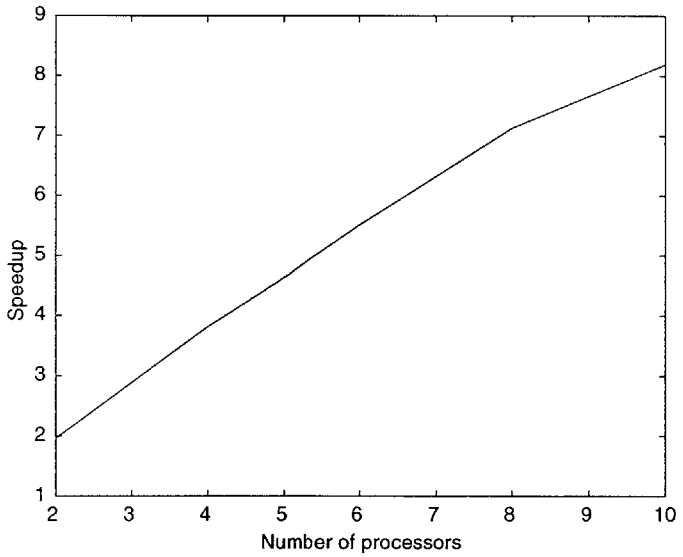

Figure 4-5: Speedup versus number of processors for a representative problem. The diffraction pattern in the focal plane of a zone plate with $\lambda = 442\,nm$, $OZW = 300\,nm$, $N = 76$ and $f = 50\,\mu m$ was calculated. Note the linear part and the slight bending down towards the right, where communication overhead starts becoming important.

Chapter 5

Simulation Results

In this chapter, we present the results of the simulations of diffraction by zone plates. The effects of the zone plate and the source parameters on the diffraction pattern in the focal plane are studied. We also present simulations of patterns and their comparison to patterns exposed on resist. Arguments for the validation of the scalar theory are discussed next.

5.1 Diffraction Pattern in the Focal Plane

In ZPAL, the spots focused by the zone plates form the pixels of the patterns which are transferred onto the substrate. We are interested in studying the geometric characteristics of these spots and how they are affected by the various design parameters in the system. For this purpose, we built a suite of simulation tools, as explained in the previous two chapters. Here, we use those tools to show the details of the diffraction pattern in the focal plane of a zone plate.

5.1.1 Effect of Zone Plate parameters

First, assume the case of a point source at infinity. This implies that a uniform plane wave is impinging on the zone plate. Then, the diffraction pattern of an amplitude

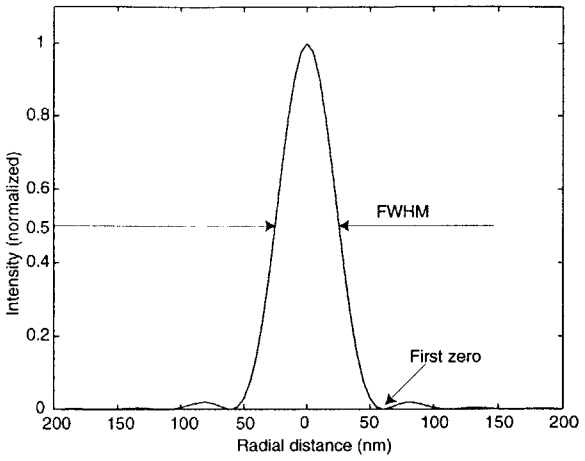

Figure 5-1: point-spread function of a zone plate with $N = 100$, $f = 220.77\,\mu m$, $OZW = 50\,nm$, and $\lambda = 4.5\,nm$. Spot-size is defined as the full-width at half-maximum (FWHM) as shown. Efficiency is defined as the ratio of the area under the curve between the first zeros to the total area.

zone plate simplifies to:

$$U(P_1) = \underbrace{\sum_{n=1}^{N-1}}_{\text{open zones}} \frac{iU_0}{\lambda} \int_{\rho=R_n}^{\rho=R_{n+1}} \int_{\theta=0}^{\theta=2\pi} \frac{exp(-iks)}{s} \frac{cos(\boldsymbol{n}, \boldsymbol{s}) - 1}{2} \rho\, d\rho\, d\theta, \qquad (5.1)$$

where (ρ, θ) is a point on the zone plate in cylindrical coordinates. We also assume that the source is essentially monochromatic. The diffraction pattern in the focal plane of the zone plate is then called its point-spread function (see Figure 5-1). All the zone plate designs for ZPAL in our research have been done using the set of Equations 2.11 and 2.12. Since this set has a reduced degree of freedom, as discussed in Chapter 2, we can only specify 3 parameters, and the 4th one is automatically fixed. In our case, the parameters chosen were OZW, N and λ, while f was fixed by the other 3 variables. For practical purposes, the only real design variables available to us are OZW and N, since the λ is fixed by the available light sources.

We can extract some important information regarding the spot-size and the background from this point-spread function. Here we define the spot-size as the full-width at half-maximum (FWHM) of the point-spread function. Below, we plot the FWHM versus the number of zones (Figure 5-2(a)) and versus the focal length (Figure 5-2(b))

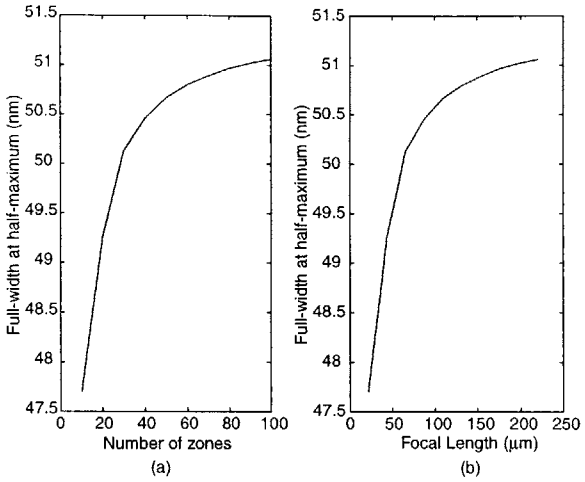

Figure 5-2: Variation of FWHM with (a) the number of zones and (b) the focal length for a zone plate with $OZW = 50\,nm$ and $\lambda = 4.5\,nm$.

for a zone plate designed to work at a wavelength of 4.5 nm and with an OZW of 50 nm. While we kept λ and OZW fixed, we varied N, and f changed correspondingly. It is interesting to note that although the variation is small, the FWHM increases slightly with both N and f. The value of the FWHM is close to the designed OZW of 50 nm.

In order to quantify the amount of energy diffracted into the background, we define the efficiency to be the ratio of the area under the point-spread function between the first zeros on either side, to the total area (see Figure 5-1).

$$\eta = \frac{\int_0^{r_1} I(\rho)\rho\, d\rho}{\int_0^{\infty} I(\rho)\rho\, d\rho}, \tag{5.2}$$

where η is the efficiency, $I(\rho)$ is the diffracted intensity at a radial distance of ρ and r_1 is the radial distance of the first zero. This efficiency is a measure of how much energy is focused into the spot compared to the total energy passing through the focal plane. The underlying diffraction process can be understood quite clearly if one looks at Figure 5-3. We can see that the incident energy is divided up among the various orders. At the first order focal plane, energy diffracted into every other order contributes to the background. Figure 5-4 (a) shows an example point-spread function, where the normalized intensity is plotted in the log scale. The plot shows clear

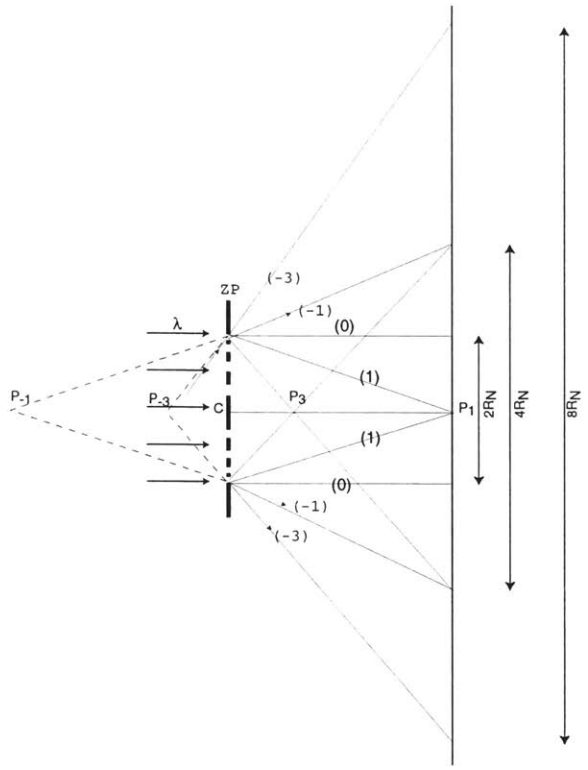

Figure 5-3: Different diffracted orders of a zone plate. P_{-1}, P_{-3}, P_3, and P_1 are the negative first, negative third, positive third and positive first order foci respectively. R_N is the radius of the zone plate. The regions of influence of the different orders are as predicted by the geometrical theory of optics.

demarcation between the diffracted orders and the positions agree well with those predicted by geometrical optics (Figure 5-3). Figure 5-4(b) shows the normalized intensity integrated over the radial spread of the diffraction pattern plotted against the radial distance. Again the regions of influence of each order are clear. It must be noted that the plot tends to go to a constant value, indicating that orders higher than 3 have negligible contributions to the total energy.

We plot the normalized efficiency, as a function of the number of zones in Figure 5-5(a) and also versus the focal length in Figure 5-5(b). Again it is interesting to note that the efficiency increases with both N and f.

Figure 5-6 suggests that the requirements for lithography of smaller spot-size (for finer feature sizes) and higher efficiency (for higher contrast) are contradictory. Figure 5-6 (a) shows the increase of the efficiency as the OZW is increased and Figure 5-6

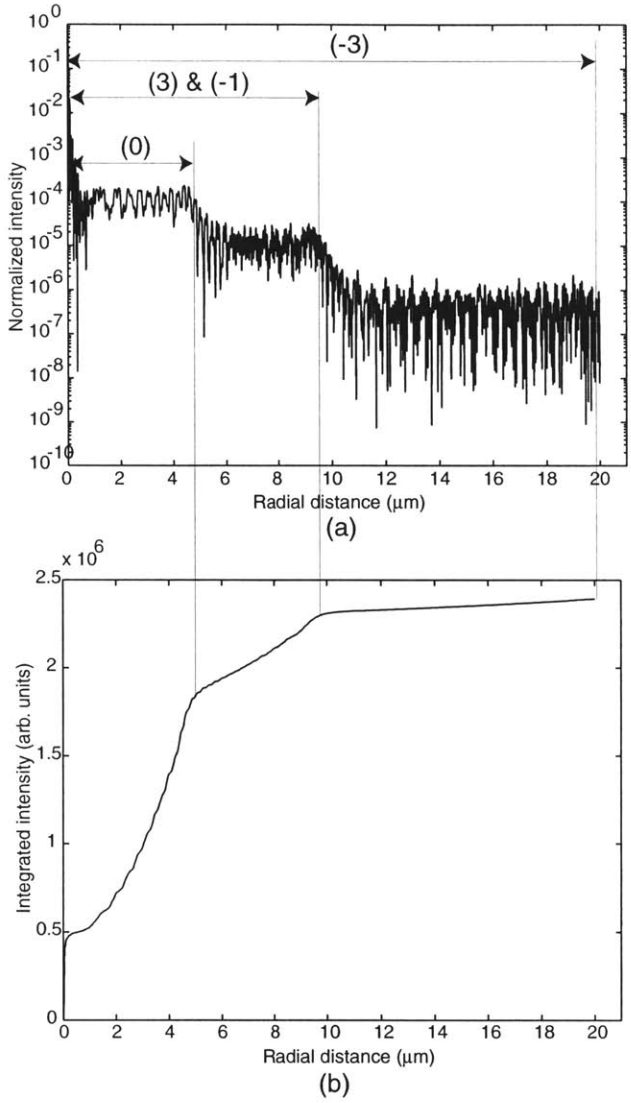

Figure 5-4: (a) Diffraction pattern with the normalized intensity plotted in the log scale. Numbers in parenthesis indicate the diffracted orders. (b) The normalized intensity integrated over its radial spread area. Both the plots show the regions of influence of the different diffracted orders. The simulation results agree with those predicted by the geometrical theory of optics. These simulations were performed for a zone plate with $\lambda = 4.5\,nm, f = 109.83\,\mu m, OZW = 50\,nm$ and $N = 50$.

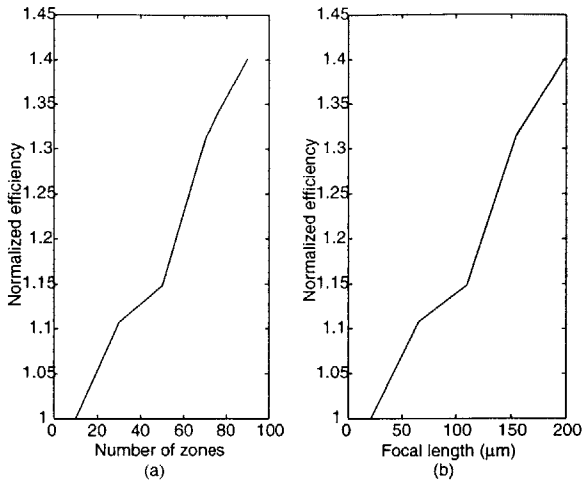

Figure 5-5: Normalized efficiency is plotted versus (a) the number of zones and (b) the focal length. The fixed parameters are $OZW = 50\,nm$ and $\lambda = 4.5\,nm$.

(b) shows a linear relation between the OZW and spot-size, as expected.

We can also calculate the diffraction pattern along the optical axis of a zone plate. The axial intensity distribution enables us to calculate the depth-of-focus (DOF) of the zone plate. We define the DOF as that axial displacement which leads to a 20% decrease in the on-axis intensity at focus [15]. In order to preserve the spot-size for ZPAL, we need to ensure that the gap between the zone plate and the substrate is within the DOF of the zone plate. Hence, the DOF becomes an important practical design consideration. Figure 5-7 shows the axial intensity distribution for a zone plate with $OZW = 50\,nm, \lambda = 4.5\,nm, f = 109.83\,\mu m$, and $N = 50$. Using the expression $DOF = \frac{4OZW^2}{\lambda}$, we can estimate the DOF to be about $2.2\,\mu m$, which is close to the value obtained in the simulation. Note that the intensity peaks at the focus. From radial intensity simulations, we know that the spot-size is at its minimum in the focal plane.

In Figure 5-8(a), we show the variation of the DOF versus the number of zones, and in Figure 5-8(b) versus the OZW. The DOF remains fairly constant until about $N = 50$, beyond which the DOF decreases as N increases. Further study need to be done to understand this behavior. As OZW increases, the DOF also increases. Again, the requirement of small spot-size seems to run counter to that of a large DOF.

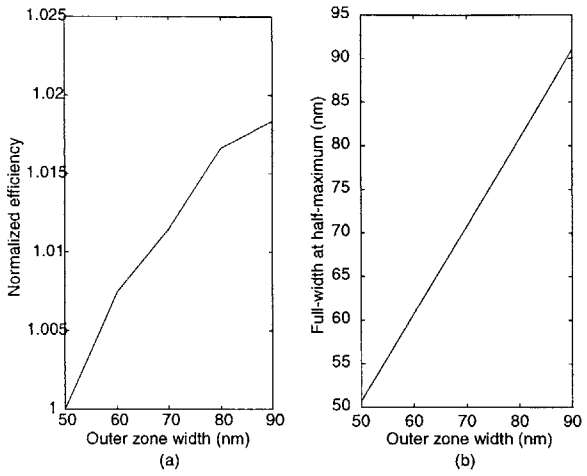

Figure 5-6: Effect of OZW on (a) normalized efficiency and (b) full-width at half-maximum. The fixed parameters are $N = 50$ and $\lambda = 4.5\,nm$.

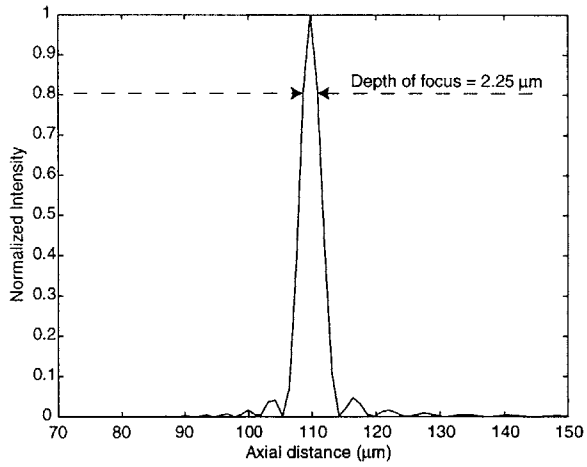

Figure 5-7: Axial intensity distribution for a zone plate with $OZW = 50\,nm, \lambda = 4.5\,nm, f = 109.83\,\mu m$, and $N = 50$.

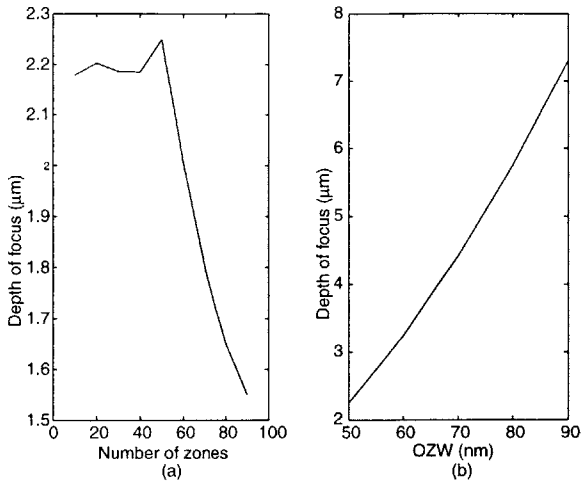

Figure 5-8: DOF variation with (a) N ($OZW = 50\,nm, \lambda = 4.5\,nm$) and (b) OZW ($N = 50, \lambda = 4.5\,nm$).

This is to be expected from the well-known approximate relation: $DOF = \frac{4OZW^2}{\lambda}$.

In order to have a clearer understanding of the role of the different zones in forming the diffracted spot, we simulated the selective illumination of certain zones of a zone plate. Figure 5-9 shows the simulated point-spread function as the zone plate is "built up" from the inner center. The central peak sharpens considerably while the intensity of the sidelobes is only slightly changed.

Figure 5-10 shows the same zone plate with a central stop of increasing radius. The stop successively covers the zones starting from the center. As the central zones are covered, the central peak sharpens further. However, the side lobe intensity is significantly increased. Thus, the central zones play an important role in reducing the background, while the outer zones cause the central peak to be sharper.

5.1.2 Effect of Source Parameters

In this section, we look at the influence of the source parameters on the diffraction pattern near the focus of the zone plate. The properties of the source depend critically on the wavelength of the radiation. Although ZPAL was envisioned initially for x-rays [1], diffractive optical elements such as zone plates can focus radiation of any wavelength. Subsequent experimental demonstrations of feasibility were performed at

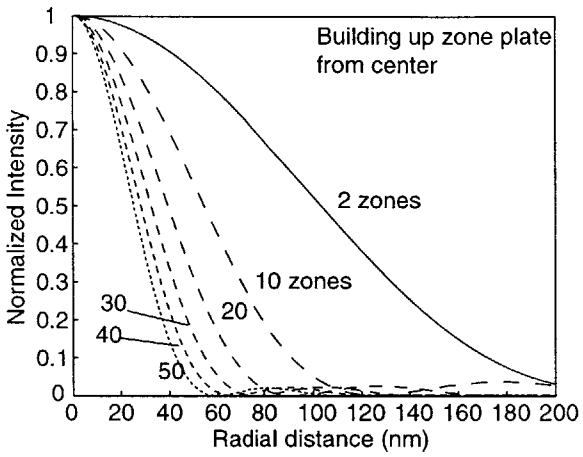

Figure 5-9: Building up a zone plate. The parameters are $N = 50, OZW = 50\,nm, \lambda = 4.5\,nm$, and $f = 109.83\,\mu m$.

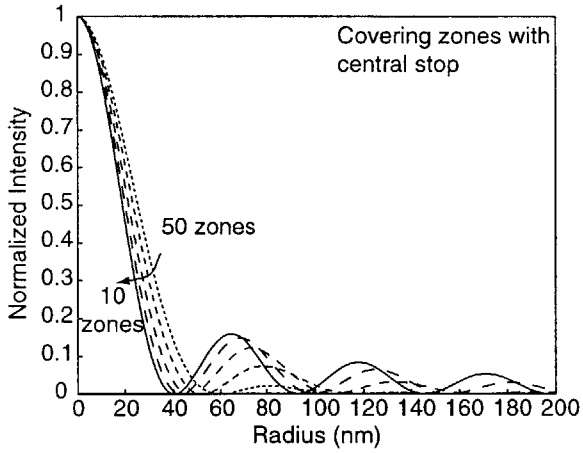

Figure 5-10: Covering the zone plate with a central stop of increasing radius. The parameters are $N = 50, OZW = 50\,nm, \lambda = 4.5\,nm$ and $f = 109.83\,\mu m$.

UV[1] [2, 5]. For UV, tabletop laser sources are available. A high degree of spatial and temporal coherence can be attained with these sources, such that they behave like perfect point sources at infinity. However, for x-rays, the situation is quite different. There are two types of x-ray sources. The first is when an electron makes a transition from a higher energy level to a level close to the nucleus, emitting an x-ray photon. This gives a line spectrum, as seen in electron bombardment of low-atomic number targets or in the plasma of low atomic-number elements. The second is by the acceleration of charged particles, such as electrons, bombarding a high atomic-number target or electrons forced to move in circular orbits in a synchrotron. This produces a continuous spectrum. Synchrotron sources have higher average intensities. The brightness of synchrotron sources can be increased by using an undulator [11]. For x-ray ZPAL, initial experiments are being performed on an electron bombardment carbon (C_K) source, emitting photons at 4.5 nm. These sources do not have perfect spatial and temporal coherence and therefore cannot be treated as monochromatic point sources.

Finite Source Size

Here, we look at the influence of a source of finite size upon the intensity distribution near the focus. As mentioned earlier, the zone plate acts essentially like a lens. The zone plate will form the image of an object. Figure 5-11 shows an extended object being imaged by a zone plate. The object distance, z and the image distance, z' are related through the lens equation:

$$\frac{1}{z} + \frac{1}{z'} = \frac{1}{f}, \tag{5.3}$$

[1]The latest experiments were performed at $442\,nm$, which is close to the boundary of visible and UV. However for the purposes of this thesis, we refer to it as UV.

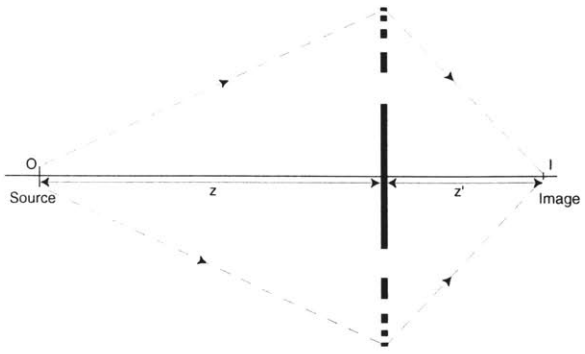

Figure 5-11: Image formation by a zone plate.

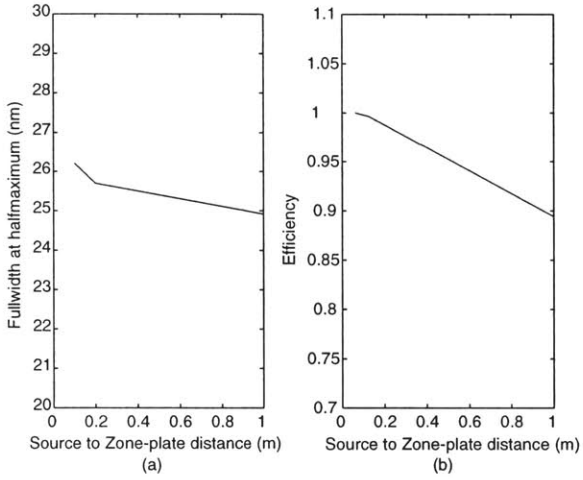

Figure 5-12: Effects of a source of finite size. (a) shows the plot of the FWHM versus the source zone plate distance. (b) shows the normalized efficiency versus the source zone plate distance. The zone plate parameters are $N = 100, OZW = 25\,nm, \lambda = 4.5\,nm$ and $f = 88\,\mu m$. Source diameter is $1mm$.

where f is the focal length of the zone plate. If the size of the object is O, the size of the image, I is given as:

$$I = O\frac{z'}{z} = O\frac{f}{z-f}. \tag{5.4}$$

To study the effect of the finite source size, we simulate the effects of a source of a given size at various distances from the zone plate.

Figure 5-12 (a) shows the FWHM at various source to zone plate distances. The demagnified image of the source convolved with the point-spread function defines this

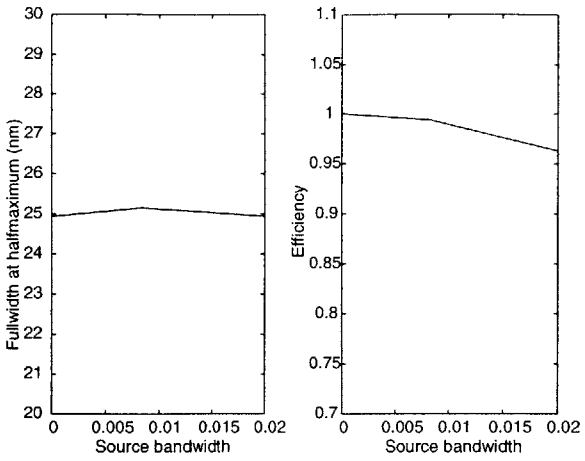

Figure 5-13: Effects of a source of finite bandwidth. (a) shows the plot of the FWHM versus source bandwidth. (b) shows the efficiency versus source bandwidth. The zone plate parameters are $N = 50, OZW = 25\,nm, \lambda = 4.5\,nm$ and $f = 27.33\,\mu m$.

FWHM. As the distance between the zone plate and the source increases, the FWHM decreases and tends to the OZW in an asymptotic manner, as the distance goes to ∞. Figure 5-12 (b) shows the efficiency as plotted against the source zone plate distance. As the source is brought closer to the zone plate, the spot-size increases, and as a consequence the fraction of the energy in the spot goes up.

Finite Source Bandwidth

In order to decouple the various influences, we make use of a perfect point source at infinity in these simulations. However, the light incident on the zone plate has a spread in wavelength. The source bandwidth is defined as the ratio of the spread in wavelength to the central wavelength.

$$BW = \frac{\Delta\lambda}{\lambda} \tag{5.5}$$

Figure 5-13 plots (a) the FWHM and (b) the normalized efficiency versus the source bandwidth. Hence 0 on the horizontal axis represents a monochromatic source. The FWHM shows a small change as the spread in wavelength is increased. The efficiency decreases slightly when the source bandwidth is increased.

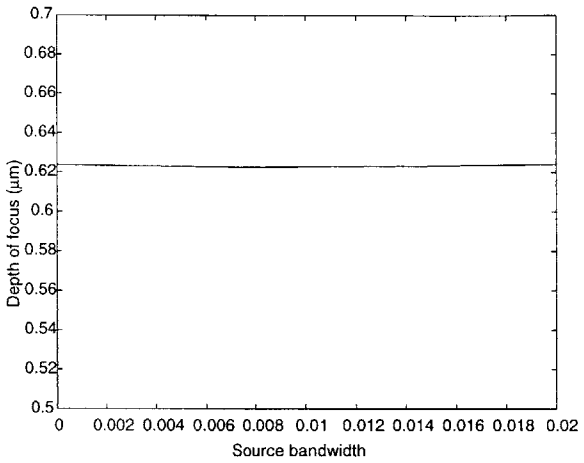

Figure 5-14: Axial effects of a source of finite bandwidth. The plot shows DOF versus source bandwidth. The zone plate parameters are $N = 50, OZW = 25\,nm, \lambda = 4.5\,nm$ and $f = 27.33\,\mu m$.

Figure 5-14 shows the plot of the DOF versus the source bandwidth. The variation in DOF is minimal.

5.2 Effects of Fabrication Errors

The previous simulations have been based on the design of a perfect zone plate. In the real world, we unfortunately are limited by the fabrication processes. In particular, we cannot specify the radii of the zones to arbitrary accuracy. There are two main possible types of errors: zone-placement errors, which give rise to narrower or wider zones, and phase-shift errors caused by errors in the etch depth while fabricating phase zone plates.

5.2.1 Zone Boundary Errors

The errors are assumed to be in the zone radii, and hence the pattern remains circularly symmetric. The case of the zone plate where alternate zones are wider and narrower are studied. This causes the opaque zones to be narrower and the transparent ones to be wider or vice-versa. The error is expressed as a percentage of the

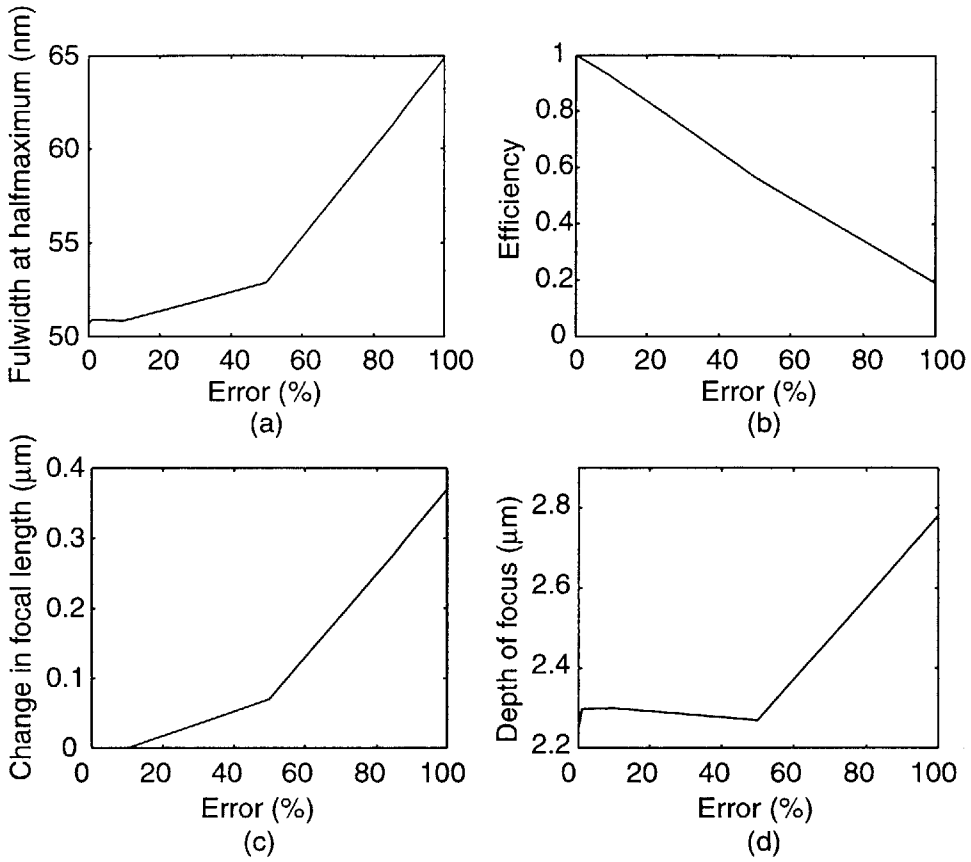

Figure 5-15: Effect of zone-boundary errors. (a) FWHM, (b) efficiency, (c) shift in focal length and (d) DOF are plotted against the error in zone radii expressed as a percentage of the OZW. The zone plate parameters are $N = 50, OZW = 50\,nm$, and $\lambda = 4.5\,nm$.

OZW of the zone plate.

$$\Delta r = \frac{R'_n - R_n}{OZW} 100, \tag{5.6}$$

where R_n and R'_n are the designed and the actual radius of the n^{th} zone.

Figure 5-15 shows the plots of (a) FWHM, (b) efficiency, (c) shift in focal length and (d) DOF versus the error. These simulations were performed for a zone plate with $N = 50, OZW = 50\,nm$, and $\lambda = 4.5\,nm$. The spot-size increases while the efficiency decreases with the error. This tends to suggest that the energy is being diverted from the first order focus. Even orders start to appear at high errors, as seen in Figure 5-16. The focal length of the zone plate changes as we include the

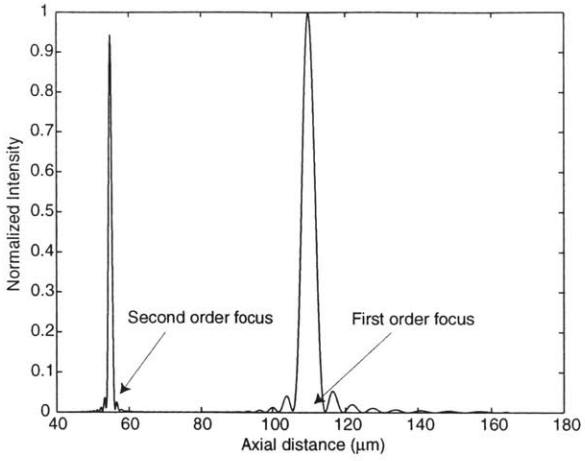

Figure 5-16: Effect of zone-boundary error on the axial intensity distribution. Note the existence of the 2nd order focus. The zone plate parameters are $N = 50, OZW = 50\,nm$, and $\lambda = 4.5\,nm$. The error was 50%.

zone boundary error. The DOF shows a slight increase with the error. Thus the most important effect of the zone boundary error is to shift some energy from the first order focus into several other (including even) orders.

5.2.2 Phase Shift Errors

In phase zone plates, alternate zones have π phase shift compared to the other zones and hence focus more of the incident radiation into the first-order focus. In order to produce this phase difference between adjacent zones, we need to etch down alternate zones and thereby create the necessary optical-path-length difference. However, the accuracy of this etch depth cannot be controlled arbitrarily. Any error in the etch depth translates into a phase shift error for the zone plate. We analyze how this phase shift error affects the various figures of merit.

Figure 5-17 (a) shows the FWHM plotted against a phase shift error, expressed as a % of π. The effect seems to be quite small. Figure 5-17 (b) shows the efficiency (normalized to the first value) as a function of the phase shift error. The efficiency decreases quite significantly as the error increases. This is seen in the increased side-lobe intensity and more energy being diverted away from the focus and into the background. It was also observed that the absolute efficiency was about 4 times

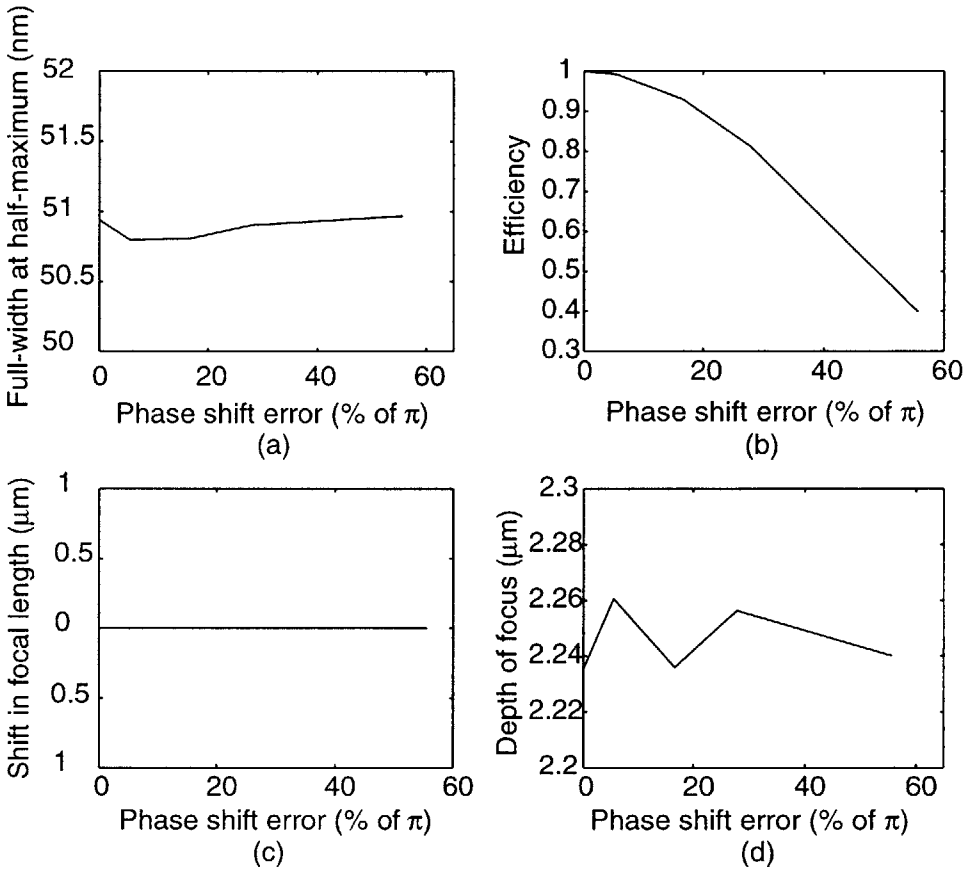

Figure 5-17: Effect of phase shift error. Figure shows (a) FWHM, (b) efficiency (normalized to the first value), (c) shift in focal length and (d) DOF versus the phase shift error, expressed as a % of π. The zone plate parameters are $N = 50, OZW = 50\,nm$, $f = 109.83\,\mu m$ and $\lambda = 4.5\,nm$.

that of an amplitude zone plate with similar parameters, as expected. Figure 5-17 (c) shows that phase shift error does not cause the focal length of the zone plate to change. This is in contrast to the zone boundary error (discussed in the previous section). Figure 5-17 (d) shows the DOF versus the phase shift error. Again, the effect is small and does not show any simple relationship.

5.3 Pattern Simulations

The diffracted intensities near the focus of the zone plate are calculated as described in the previous chapter. Each focused spot forms a pixel of the pattern to be transferred onto the substrate. The substrate is coated with radiation sensitive resist. This is usually an organic polymer that reacts to incident light in a particular way. In the case of negative resist, the incident light makes it more resistant to developing. For a positive resist, the light causes it to be less resistant to developing. Thus any pattern can be transferred onto the substrate. In addition to several desirable properties [26], we would like the resist to have very high contrast. This means that for any given thickness of resist, we would like the resist to behave in a binary manner, i.e., the entire resist underneath a pixel area should react completely above a certain threshold incident light energy and not react at all below it. Although in practice no resist has perfect contrast, there are several such as PMMA which approximate this behavior quite well. This preliminary pattern analysis uses a binary response of the resist to define the patterns on the substrate.

In order to simulate the exposure, the substrate is divided into a grid of sub-pixel size, where a pixel is the spot-size (or FWHM). For every point on this grid, we can determine the intensity contribution it receives from every exposed pixel on the substrate, with a knowledge of the point-spread function of the zone plate. Since intensity adds incoherently in resist, all such intensity contributions are added up to obtain the total intensity received by that point. This is repeated for all the points in the grid.

This simulation process is illustrated in Figure 5-18. Since the point-spread func-

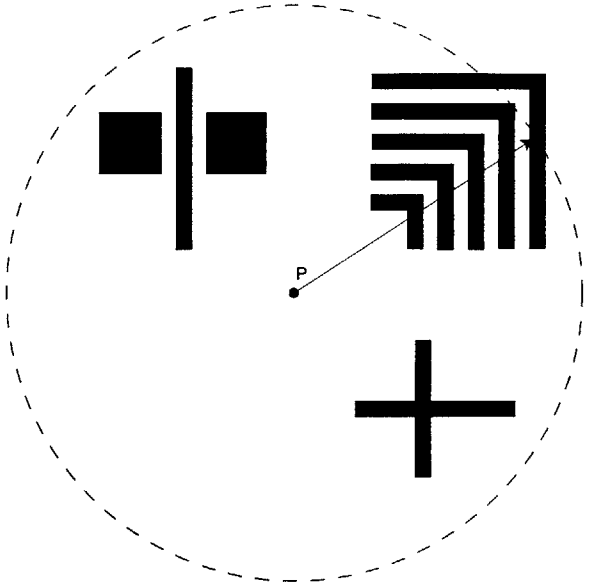

Figure 5-18: Simulating a pattern. Contribution from all the exposed pixels (black regions) at point P are added up to obtain the total intensity received by P. Since the point-spread function is radially symmetric, we can use circles of increasing radii to do this calculation.

tion is radially symmetric, we can add the contributions from all the exposed pixels on a circle of a given radius at the central point P and repeat this for circles with increasing radii until the contribution becomes negligible. Finally, by employing a binary clipping model of the resist, we can take a contour plot of the intensity values throughout the substrate and obtain a simulated pattern.

5.3.1 UV ZPAL Experimental Setup

As mentioned in Chapter 1, the preliminary investigations into ZPAL were conducted at a wavelength of 442 nm. The multiplexing of the beamlets was performed by the Texas Instruments micromirror array. A 3 by 3 array of phase zone plates was fabricated on a quartz substrate. These were written by Darío Gil using the electron-beam lithography tool at the NanoStructures Laboratory. The design parameters for the set of zone plates used in these experiments were $N = 76, OZW = 336\,nm, \lambda = 442\,nm$ and $f = 50.94\,\mu m$. The patterns were exposed in Shipley 1813 photoresist, which was spin-coated on a silicon wafer. A photograph of the setup is shown in

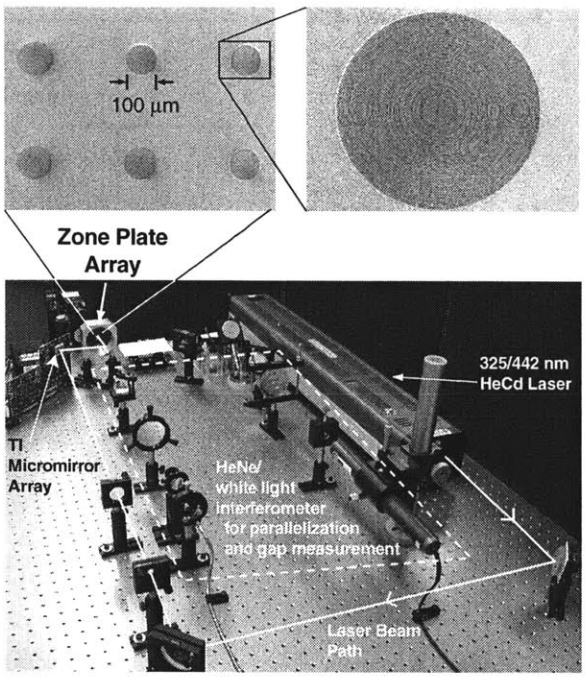

Figure 5-19: A photograph of the UV ZPAL setup. Top left inset shows a part of the zone plate array. Top right inset shows one zone plate.

Figure 5-19.

The patterns were first drawn up in a high level drawing program called Nanowriter in the kic format. This program was written by Mitch Meinhold at the NanoStructures laboratory in MIT. The objective of the experiment was to show the feasibility of parallel writing using ZPAL. Since we had an array of 3 by 3 zone plates, we drew 9 different patterns to be addressed by the 9 zone plates simultaneously. The zone-plate unit cell is defined as the area on the wafer addressed by the zone plate. The patterns are shown in Figure 5-20. The horizontal and vertical extents of the zone-plate unit cells are not equal. This is to match the same mismatch in the fabricated zone plate array. This mismatch was, in turn, introduced to account for foreshortening due to oblique incidence of the light on the micromirrors used for multiplexing [12].

Nanowriter can output files in the kic format. The patterns were saved in kic format and a *kictozpal* translator was used to convert the files to a format suitable

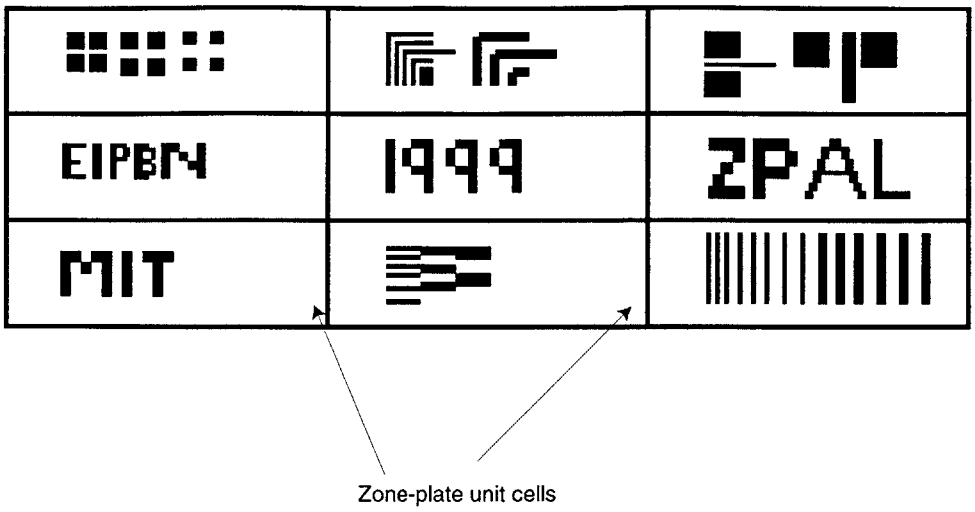

Figure 5-20: Nine different patterns were drawn in Nanowriter. The horizontal and vertical lines demarcate the zone-plate unit cells. Note that each unit cell has to address a different pattern, which would demonstrate parallel writing. The drawing is not to scale.

for the ZPAL system. The details of this translation and other system software are discussed later in this chapter. After exposure and developing, the patterns were formed on resist. Scanning electron micrographs (SEMs) of these patterns are shown in Figure 5-21. The zone-plate unit cells are demarcated by the dotted white lines. The X and Y extent of the zone-plate unit cell correspond to the X and Y distances between zone plates in the array.

The same kic file for these patterns were also used to perform simulations. The simulation software includes code to translate the kic files to a raw exposed pixel format suitable for the simulations. The point-spread function of the zone plate with the designed parameters: $\lambda = 442\,nm, N = 76, OZW = 336\,nm$ and $f = 50.94\,\mu m$, with a π phase shift in the alternate zones was calculated and is shown in Figure 5-22.

The simulated spot matches the measured one at a resist clipping level of 0.42. This is quite close to the FWHM, which corresponds to a clipping level of 0.5. The model of diffraction of the zone plate and the binary resist development seem to be reliable in this case. The slightly larger value of the measured spot compared to the designed OZW maybe due to the fact that several spots were exposed in reasonably close proximity, leading to some background contribution to the spots.

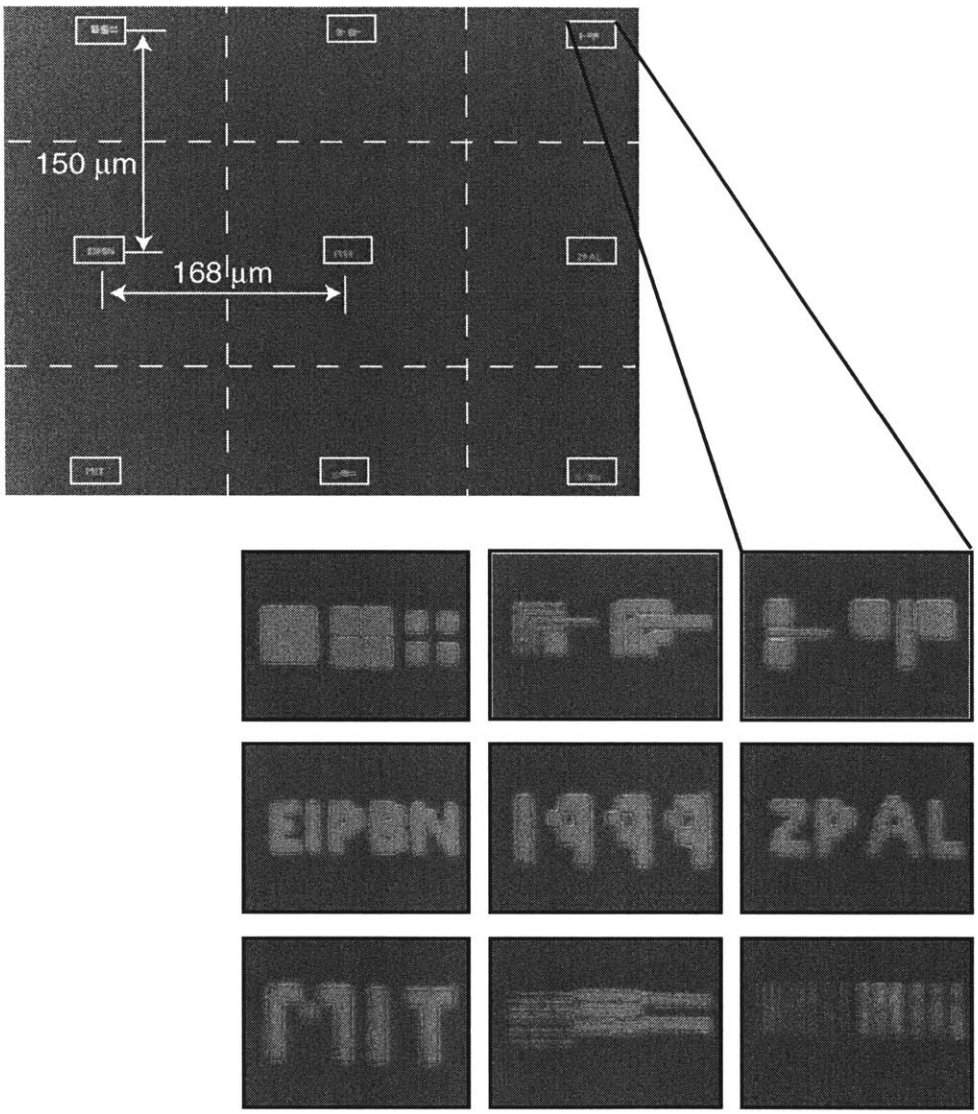

Figure 5-21: Scanning electron micrographs (SEMs) of 9 different patterns written in parallel using UV ZPAL. Note the zone-plate unit cells marked by the dotted white lines. The X and Y spacing of the unit cells correspond to the X and Y spacings in the zone plate array.

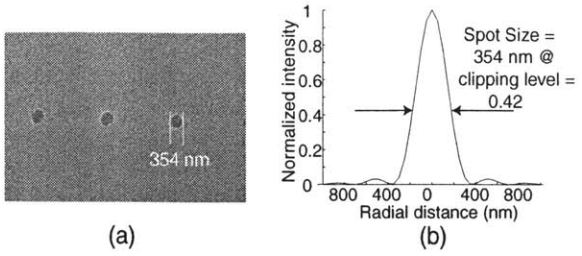

Figure 5-22: (a) SEM of individual spots exposed in resist using a phase zone plate with parameters: $\lambda = 442\,nm, N = 76, OZW = 336\,nm$ and $f = 50.94\,\mu m$. (b) Simulated point-spreadfunction of the same zone plate.

Magnified SEMs of two patterns from Figure 5-21 are shown in Figure 5-23 and these are compared to their corresponding simulations. Note that the radius of curvature of the corners in the SEMs corresponds to a spot size of about $330\,nm$. This shows the fidelity of the printed patterns. Figure 5-23 (a) shows a pattern of a line between two pads to demonstrate the proximity effect. Figure 5-23 (b) shows a nested-L pattern, again to demonstrate proximity effects. Figure 5-23 (c) and (d) show the simulations of the patterns in (a) and (b) respectively. With a fixed resist clipping level, corresponding linewidth measurements agree quite well. Note also that the SEM has a measurement error of about $\pm 25\,nm$ at this magnification.

Zone plates can be used to focus light of any radiation. In order to achieve the lithographic limit in patterning, one needs to go to smaller wavelengths. Years of research at the NanoStructures Laboratory and elsewhere seems to suggest some obvious advantages to using the 4.5 nm photon for lithography [1, 5]. Earlier work has shown patterning of very small features (sub-20 nm) using the 4.5n x-rays [27]. Theoretical analysis has also shown high contrast for patterns exposed in resist with 4.5 nm x-rays [28]. Amplitude zone plates for x-rays were fabricated by Dr. Erik Anderson using the nanowriter electron-beam lithography tool at the Lawrence Berkeley Laboratory. The opaque zones were electroplated nickel of 60 nm thickness and the zone plate was fabricated on a 110- nm-thick SiNx membrane. These are shown in Figure 5-24. These zone plates were designed with $N = 50, OZW = 45\,nm, f = 100\,\mu m$ and $\lambda = 4.5\,nm$.

The source in our x-ray ZPAL experimental setup is a carbon target, bombarded

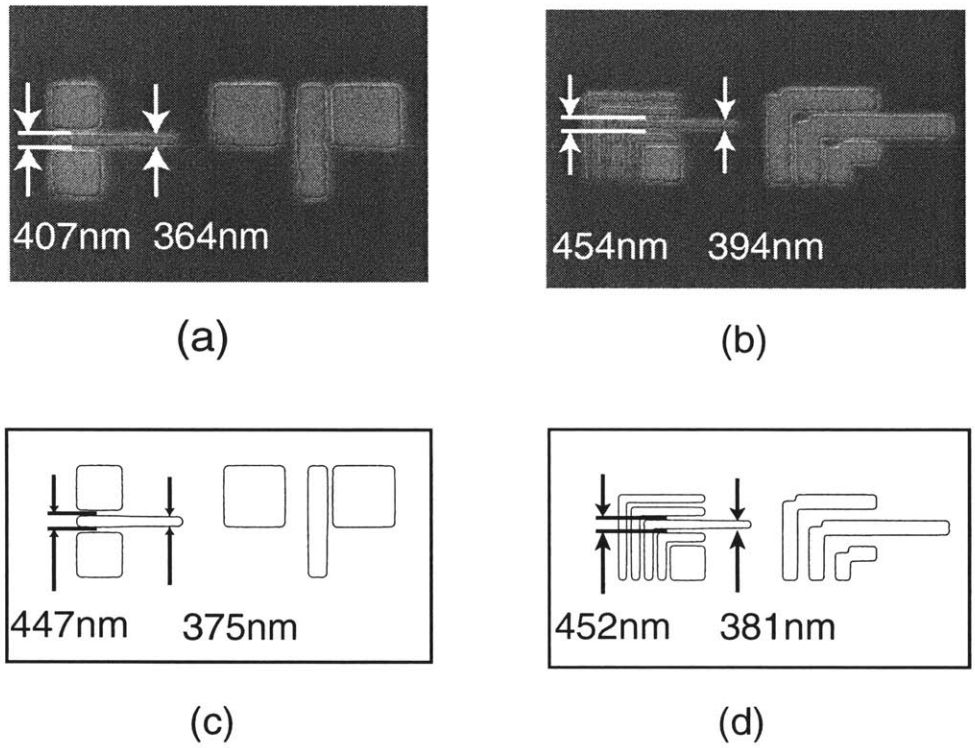

Figure 5-23: (a) A magnified SEM of one pattern from Figure 5-21. Note proximity effect broadening of the line due to the adjacent pads. (b) A magnified SEM of a nested-L pattern from Figure 5-21. Again the proximity effect tends to make the extended portion of the line narrower. Note that the notch at the edge is reproduced faithfully. (c) Simulation of the pattern in (a). (d) Simulation of the pattern in (b). Allowing for an SEM measurement error of $\pm 25\,nm$, they are in good agreement.

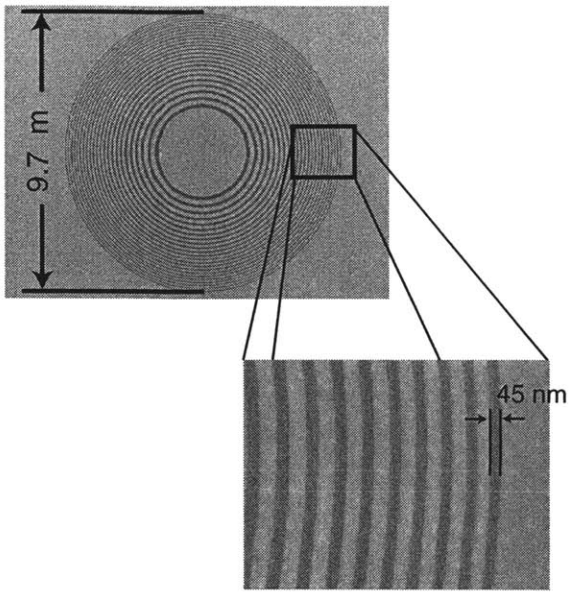

Figure 5-24: SEM of the x-ray amplitude zone plates fabricated by Dr. Erik Anderson at Lawrence Berkeley Laboratories. The design parameters are $N = 50, OZW = 45\,nm, f = 100\,\mu m$ and $\lambda = 4.5\,nm$.

by electrons. The source has a measured diameter of about 0.5mm. With a distance of about 1.5m between the source and zone plate, this corresponds to a demagnified image size of about 33 nm diameter. Using these design parameters, the point-spread function was simulated and is shown in Figure 5-25(a). The simulated FWHM corresponds very well to the expected one of about 55 nm (obtained by convolving the demagnified image of the source with the diffraction-limited spot). Figure 5-25 (b) shows a proximity test pattern simulated with the point-spread function in (a). The significant proximity effect broadening at the ends of the line is mainly due to the finite size of the source. Simulations with a perfect point source show much less proximity effect.

Fabrication of zone plates has become quite mature recently. Researchers have made zone plates with sub-20 nm resolution for use in x-ray microscopy and spectromicroscopy [29]. This is the ultimate direction of x-ray ZPAL in order to obtain sub-50 nm features. We simulated the diffraction of a zone plate with $N = 100, OZW = 25\,nm, \lambda = 4.5\,nm$ and $f = 50.94\,\mu m$. In the following simulations, we assumed a

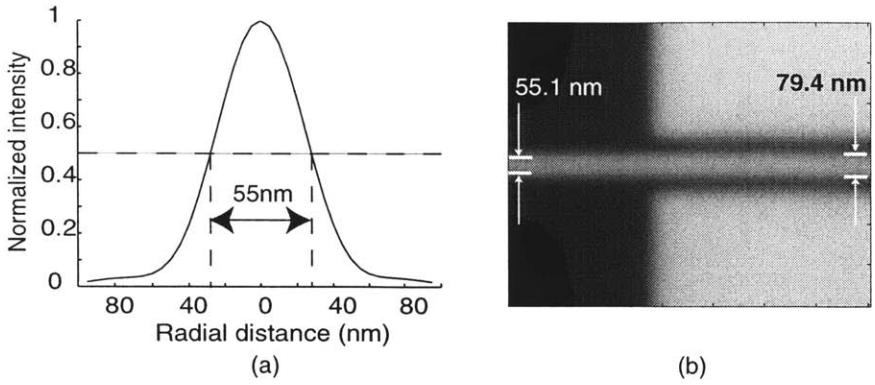

Figure 5-25: (a)Simulated point-spread function of the zone plate in Figure 5-24. The source diameter was 0.5mm; this corresponds to an expected FWHM of about 55 nm. (b)Simulated proximity effect test pattern. Significant line broadening is due to the finite source size.

perfectly collimated incident beam with zero bandwidth.

Figure 5-26(a) shows a proximity effect test pattern of a line between two big pads. The linewidth is close to the designed value of $OZW = 25\,nm$. A small proximity effect is observed. Figure 5-26(b) shows a simulated nested-L pattern. Again the proximity effect shows up but is reasonable due to the choice of a collimated source. These simulations indicate that patterns at linewidths of about 25 nm can be written using x-ray ZPAL.

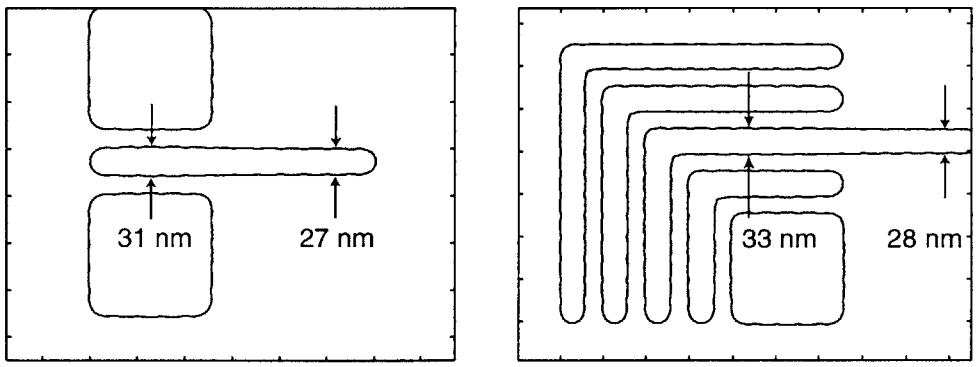

Figure 5-26: (a) Simulated proximity effect test pattern. Note the small broadening of the line in the region between the pads. (b) Simulated nested-L pattern. Again a small proximity effect is seen. The parameters of the zone plate were $N = 100, \lambda = 4.5, OZW = 25\,nm$ and $f = 50.94\,\mu m$. Note that the linewidths are close to the designed value.

5.4 Validation of Scalar Theory

The Fresnel-Kirchhoff diffraction theory is approximate in the sense that extra line integrals are necessary to compute diffraction behavior along the zone edges. However, studies have shown that the error introduced is small when the focus (observation point) is many wavelengths away from the zone plate [30]. Beynon *et al.* have compared near field computations using the Fresnel-Kirchhoff equation to the solution of Sommerfeld for an infinite perfectly conducting half-plane and found very good agreement.

The approximations inherent in the scalar theory cause it to give erroneous results for small feature sizes (compared to the wavelength) and large aspect ratios. This has been investigated by Pommet *et al.* [31]. They compared the diffraction efficiencies of gratings obtained by a scalar ray tracing technique to the exact solution provided by the Rigorous Coupled Wave Theory (RCWT) [32]. The RCWT is an exact solution of vector Maxwell's equations for infinite periodic structures. The study concluded that for profiles with equal lines and spaces, the grating period, rather than the minimum feature size determines the accuracy of the calculation. Furthermore, their simulations showed that the error for single-level diffractive elements with a 50% duty cycle was very small, irrespective of the feature size. In the case of zone plates, the outer zones are more prone to error because of the smaller feature sizes, compared to the wavelength. However, locally, a zone plate looks very much like a grating with a 50% duty cycle near the outer zones. This is illustrated in a magnified plot of the outer zones for our designed zone plate with parameters: $N = 76, OZW = 336\,nm, \lambda = 442\,nm$ and $f = 50.94\,\mu m$ in Figure 5-27. Hence, the study by Pommet et. al. suggests that for this zone plate the scalar theory would give very good results even though the minimum feature sizes are sub-wavelength. This is corroborated by our earlier comparison of the simulated patterns to patterns exposed in resist.

Another important consideration we have overlooked in the simulations is the fact that the zone plate has a finite thickness. This causes the zones to look like truncated waveguides. Incident radiation can then couple to many modes within

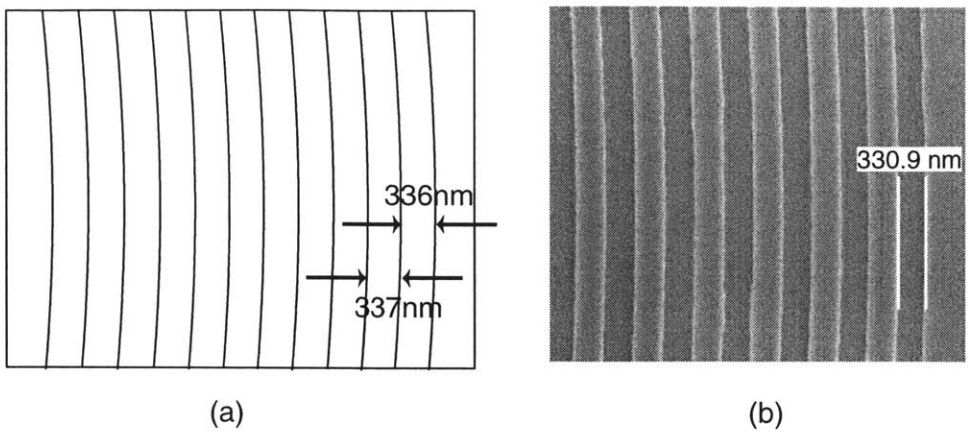

Figure 5-27: (a)Designed outer zones of a zone plate with parameters: $N = 76, OZW = 336\,nm, \lambda = 442\,nm$ and $f = 50.94\,\mu m$. (b) Scanning electron micrograph of the fabricated phase zone plate with the same parameters. Note that locally the outer zones look periodic with a 50% duty cycle.

these waveguide-like structures, thereby changing the point-spread function from a simple thin lens approximation. Maser et. al. have studied this effect using the coupled wave theory [33]. They observe that the diffraction behavior through a zone plate varies from the "optically thin" regime in the center to an "optically thick" regime at the edges. Numerical simulations were used to characterize these regions.

Figure 5-28 shows the refractive index variation along the radial direction in the outer zones of a zone plate. Locally, this region is treated as an infinite grating in the coupled wave analysis. Two parameters are defined to characterize the diffraction properties of this region.

$$\Omega = \frac{2}{\epsilon_1}\frac{\lambda^2}{\Lambda^2} \tag{5.7}$$

$$Q' = \frac{2\pi}{\epsilon_0}\frac{\lambda}{\Lambda}\frac{z}{\Lambda}, \tag{5.8}$$

where the following are defined as shown in the Figure 5-28: λ is the wavelength of light, ϵ_0 is the average refractive index in the region, ϵ_1 is the refractive index of the modulation depth of the region, z is the thickness and Λ is the period of the local grating. Ω is the structure parameter and Q' is the thickness parameter of the region.

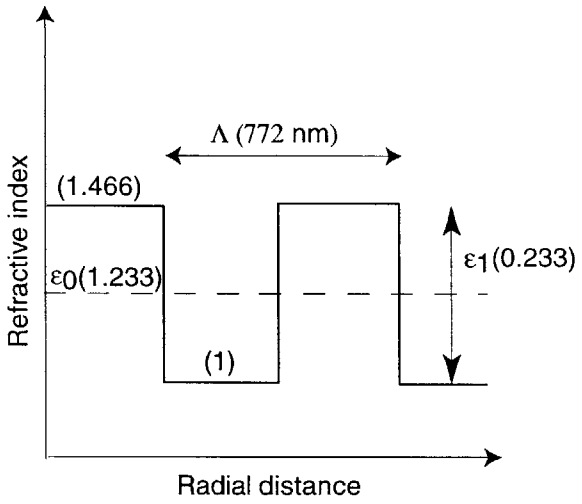

Figure 5-28: Refractive index profile of outer zones of a zone plate. Locally, the profile is treated as that of a grating in coupled wave analysis. The numbers in parenthesis indicate the designed numbers for the fabricated zone plates.

The normalized thickness, ν can be written as:

$$\nu = \frac{Q'}{2\Omega} \tag{5.9}$$

The criterion for optically thin gratings is that $Q'\nu \leqslant 1$. For optically thick gratings, the condition is that $\Omega \geqslant 10$ and $Q' > 1$. For thin gratings, a geometrical approach such as the Fresnel-Kirchhoff method should give accurate results, whereas for thick gratings, one needs to apply the Bragg condition and use the RCWT to obtain accurate results. In the case of the outer zones of the zone plates used in the experiments, the parameters had the following values [12]:

$$z = 474\,nm$$

$$\epsilon_0 = 1.233$$

$$\epsilon_1 = 0.466$$

$$\Lambda = 772\,nm$$

$$\text{Equation } 5.7 \Rightarrow \Omega = 1.8567 \leqslant 10$$

$$\text{Equation } 5.8 \Rightarrow Q' = 2.3640$$

$$\Rightarrow \nu = 0.6366$$

$$\Rightarrow Q'\nu = 1.5049 \geqslant 1, \tag{5.10}$$

which implies that the fabricated zone plates are neither optically thin nor thick. Usually this regime is characterized by complex diffraction behavior. However, in our case, the product $Q'\nu$ is not very far from 1 and $\Omega < 10$. And the corroboration with the experimental results seem to indicate that the simulations do give reasonable results. However, in order to pursue aggressive NA zone plates in the future, we intend to implement a simulation tool to solve the full vector Maxwell's equations using a finite-difference time-domain approach [34].

Chapter 6

X-ray Source Simulations

In this chapter, we introduce the electrodynamical equations used to simulate the electron-bombardment x-ray source. We present simulation results of the source-size for various source designs. Most of the work presented in this chapter was done in collaboration with Alex Bernstein.

6.1 Electron-bombardment x-ray Source

For x-ray ZPAL, we are using a carbon electron-bombardment source which has a sharp peak at the 4.5 nm C_k wavelength. Although the source does not have high x-ray flux as compared to a synchrotron source, it is compact and much less expensive. Hence, it is suitable for research purposes in our laboratory. X-rays are generated when the target material is bombarded by electrons at a high energy. The electrons are generated by thermionic emission from a tungsten filament, through which a large current is passed. These electrons are accelerated by static electric fields. Some of the electrons colliding into the target atoms knock out some inner-shell electrons, creating empty levels close to the nucleus. The atom then relaxes by causing an outer electron to transit to the inner level. The energy lost by this transiting electron is released as an x-ray photon. This process is illustrated in Figure 6-1. The characteristics and efficiency of this emission process have been discussed previously [35, 36, 37].

In this project, we are interested in studying how the electrons are accelerated

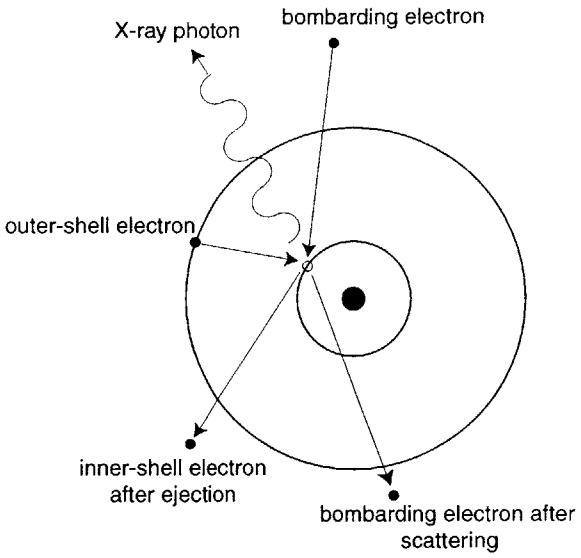

Figure 6-1: x-ray emission by an electron bombarding a target atom. An inner-shell electron is ejected and the empty level is filled by an outer-shell electron. The energy lost by the outer-shell electron is released as an x-ray photon.

using focusing electrodes. As mentioned in earlier chapters, we desire a small source size with high flux in x-ray ZPAL. Once we understand the electron trajectories in the static accelerating fields, we can design the fields to focus the electrons to a smaller spot. When the electrons bombard the target on a smaller area, we can expect to see a smaller source of x-rays as well as higher brightness due to the increased energy density.

6.2 Electrodynamics

In order to compute the electron trajectories, we begin with the electrostatic fields existing in space. Using one of Maxwell's equations:

$$\nabla \cdot (\epsilon \boldsymbol{E}) = \rho \tag{6.1}$$

and the relation:

$$\boldsymbol{E} = -\nabla V, \tag{6.2}$$

where $\boldsymbol{E}$ is the electric field, V is the electrostatic potential, ϵ is the dielectric constant and ρ is the space-charge density, we can obtain the Poisson equation:

$$-\boldsymbol{\nabla} \cdot (\epsilon \boldsymbol{\nabla} V) = \rho. \tag{6.3}$$

The x-ray source has radial symmetry which is used to reduce the dimensionality of the problem from 3 to 2. This is important since the PDE toolbox in Matlab can only handle 2 dimensional problems. Using the radial symmetry, the Poisson equation in cylindrical coordinates becomes [38]

$$\frac{1}{r}\frac{\partial}{\partial r}(r\epsilon\frac{\partial V}{\partial r}) + \frac{\partial}{\partial z}(\epsilon\frac{\partial V}{\partial z}) = \rho. \tag{6.4}$$

If we assume charge-free space, $\rho = 0$ and multiplying through by r, we get

$$\frac{\partial}{\partial r}(r\epsilon\frac{\partial V}{\partial r}) + \frac{\partial}{\partial z}(r\epsilon\frac{\partial V}{\partial z}) = 0, \tag{6.5}$$

$$\Rightarrow \boldsymbol{\nabla}_{\boldsymbol{rz}} \cdot (r\epsilon \boldsymbol{\nabla}_{\boldsymbol{rz}} V) = 0, \tag{6.6}$$

where $\boldsymbol{\nabla}_{\boldsymbol{rz}} = \frac{\partial}{\partial r}r + \frac{\partial}{\partial z}z$. Then, by redefining ϵ as $\epsilon' = r\epsilon$, we can rewrite the Poisson equation as

$$\boldsymbol{\nabla}_{\boldsymbol{rz}} . (\epsilon' \boldsymbol{\nabla}_{\boldsymbol{rz}} V) = 0. \tag{6.7}$$

Once the boundary conditions are specified, this equation can be solved using the PDE toolbox in Matlab for V. And by using 6.2, we can determine the electric field in the region of interest. The boundary conditions for electrostatic problems are of two kinds: Dirichlet or Neumann [39]. For Dirichlet conditions, the potential V is specified on the boundary. For Neumann conditions, the surface charge is specified on the boundary. The Neumann condition is used along the axis of circular symmetry by specifying the surface charge to be zero, whereas the Dirichlet condition is specified on all other boundaries.

In order to determine the dynamic behavior of the electrons in this space of static

fields, we use the Lorentz force equation:

$$\boldsymbol{F} = -e(\boldsymbol{E} + \boldsymbol{v} \times \boldsymbol{B}). \tag{6.8}$$

The effect of the magnetic field is neglected. The magnetic field can arise from either the filament which carries current or the motion of the electrons themselves. In the former, the filament has only one loop and has very small inductance. This implies that the magnetic field produced by the filament is tiny. In the case of the accelerated electrons too, the inductance effects of individual electrons is truly negligible. The dynamical equation can be written in terms of the scalar components.

$$\frac{dv_x}{dt} = \frac{-e}{m} E_x \tag{6.9}$$

$$v_x = \frac{dx}{dt} \tag{6.10}$$

$$\frac{dv_y}{dt} = \frac{-e}{m} E_y \tag{6.11}$$

$$v_y = \frac{dy}{dt}. \tag{6.12}$$

Once the initial condition is specified, the above 4 ordinary differential equations can be solved in Matlab for the electron trajectories (x, y). The initial condition consists of the direction and the speed with which an electron is thermionically ejected from the hot filament. It can be shown that most thermionic electrons are ejected normal to the surface [40]. The energy at which the electron is emitted is determined by the workfunction of the material of the filament and the filament temperature. However, the electrons are accelerated to very high velocities by the static fields and the simulations indicated that the choice of the initial speed was not critical to the results. The trajectories were followed until the electron hits the target surface. This computation was repeated for several electrons emitting from random points on the filament in order to get a statistical measurement. Then, we measure the number of electrons striking the target as a function of the radial distance from the center. If we assume a direct correlation between the incident electrons and emitted x-ray photons, the plot gives information regarding the size of the x-ray source, as well as

the emitted x-ray flux.

6.3 Simulation Results

Measurements of the x-ray source (Head 2) in the NanoStructures Laboratory were made (Appendix B). This source had a copper target, but the design is similar to the Carbon target source. Figure 6-2 shows a cross-section of the source.

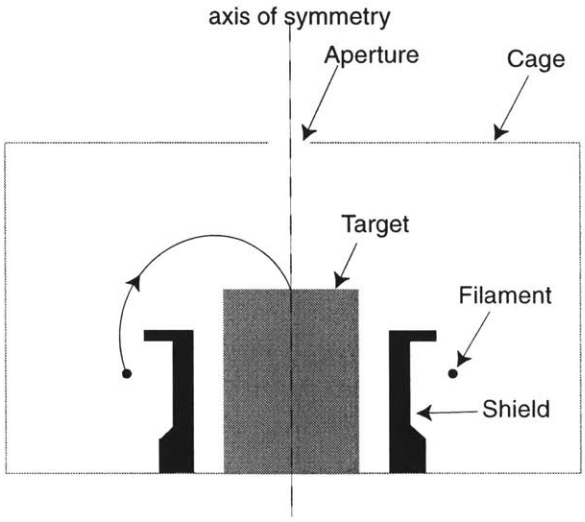

Figure 6-2: Electron-bombardment x-ray source. Electrons are thermionically ejected out of the filament and accelerated to the target surface. x-rays are emitted through the aperture above the target. The target is at ground and all other parts are at 5-8 keV. The shields (in black) are for protecting the target from contamination from the filament.

The target is held at ground while the cage and everything else is at 5-8 keV. Current is passed through the filament to heat it. The thermionic electrons are then accelerated by the static fields to the target. After they collide with the target, x-ray photons are emitted through the aperture at the top. The shields are used to protect the target from contamination due to material evaporation from the filament. The shield ensures that there is no direct line-of-sight between the target and the filament. The electrons are focused on the target by moving the target in the vertical direction.

First, the field computations were carried out using this design in Matlab. Due to the symmetry, only one half of the system need to be used for the computations.

Figure 6-3(a) shows the cross-section of the system with the generated mesh points. Note that the software automatically detects the sharp edges and creates denser mesh points there. Figure 6-3(b) shows the computed electrostatic potential values. The contours go from 0 near the target to 8kV near the cage. The lensing effect of the fields which focuses the electrons is clearly evident.

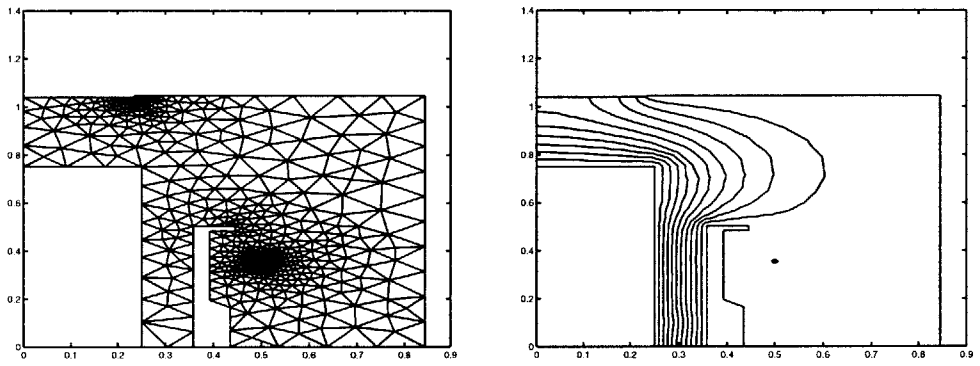

Figure 6-3: (a) Mesh generated in Matlab for the existing x-ray source. The axes are in inches. (b) Electrostatic potential contour lines for the existing x-ray source. The target is maintained at 0V, while everything else is at 8kV. The contours go from 0V near the target to 8kV near the cage.

Using the electrodynamical equations, we can compute the trajectories of the electrons emitted from the filament. Figure 6-4 shows these trajectories. Each trajectory is computed individually and the point on the filament from which the electron is emitted is randomly chosen for each. The electron trajectories end on the target surface, forming a focused spot. The initial speed of the electrons did not affect the trajectories.

By counting the number of electrons striking every point on the target surface, we can quantify the focus. Figure 6-5 shows the two positions of the target for two different foci. This was confirmed by experiment and the distance between the positions of the target for the two foci was close to the calculated value. Figure 6-6(a) and (b) show the electron distributions on the target surface for the two foci. The bar on each figure is a measure of the number of electrons hitting the target surface. This number is proportional to the x-ray flux.

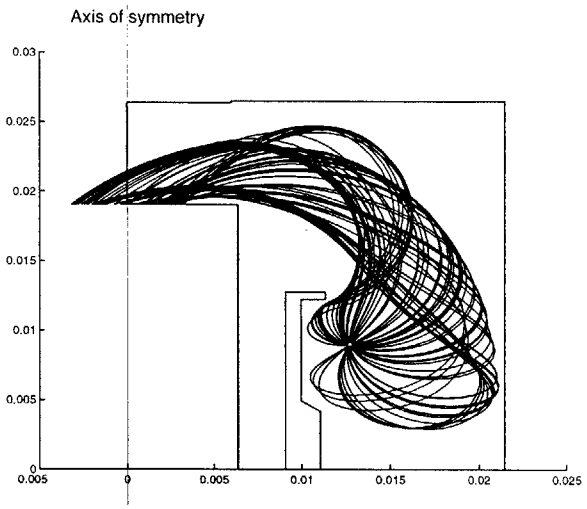

Figure 6-4: Computed trajectories for the existing x-ray source. The axis markings are in inches. For each trajectory the point on the filament from which the electron is emitted is chosen randomly. The initial velocity of the electrons was chosen to be 1.35e5 m/s normal to the surface of the filament, however this does not affect the trajectories.

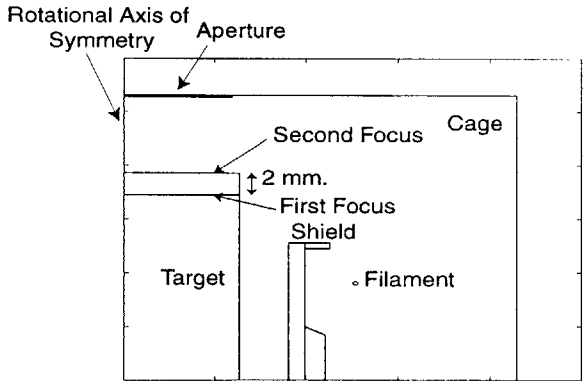

Figure 6-5: (a) Shows the two positions of the target for the two foci. (b) First focus. (c) Second focus.

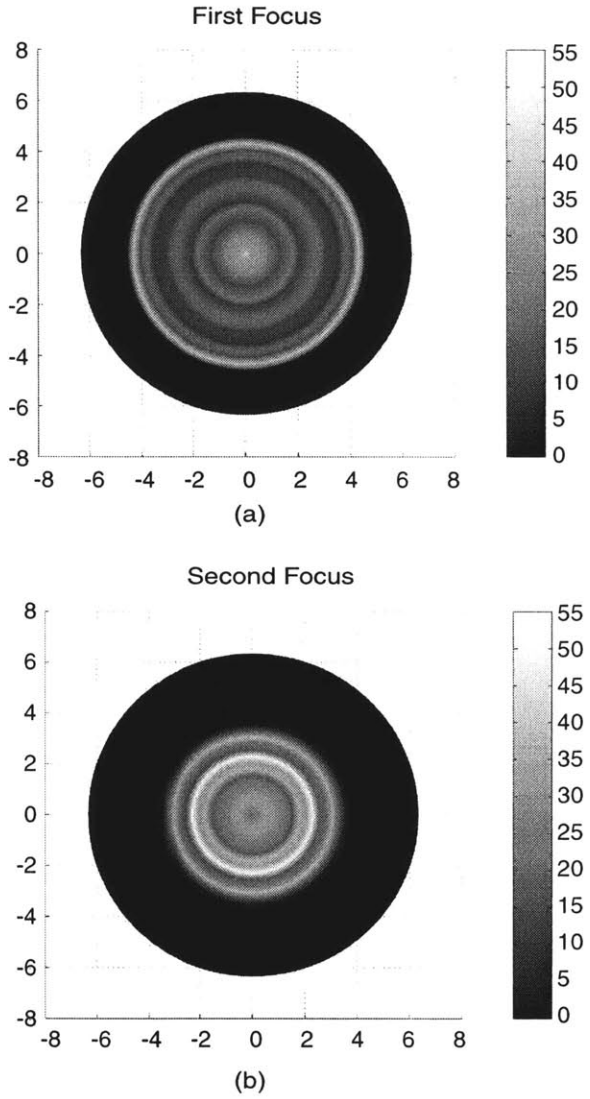

Figure 6-6: (a) Electron distribution on the target surface for the first focus, and (b) the same for the second focus. The spatial dimensions are in mils. The graybar gives actual number of electrons.

We would like to obtain a smaller focus for the x-ray source. Several designs for the focusing electrodes were studied. The main idea was to use focusing electrodes to sharpen the trajectories and also to move the filament towards that target surface. It was also important not to have a direct line-of-sight between the target and the filament to prevent contamination. The cross-section of one half of the new design for the source is shown in Figure 6-7. The extra electrodes provide a tighter focus. Note that the target is completely shielded from the filament.

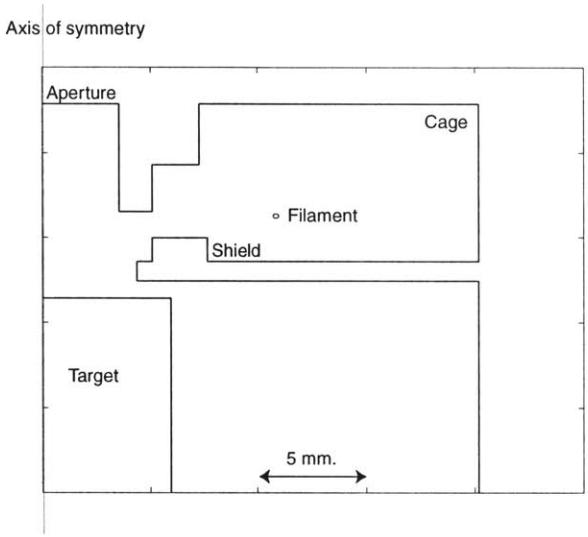

Figure 6-7: Design of improved x-ray source. The extra electrode causes the electrons to focus to a smaller spot on the target surface. The target is completely shielded from the filament.

Figure 6-8(a) shows the mesh generated for the new source design. Figure 6-8(b) shows the computed electrostatic potential contour lines extending from 0V near the target to 8kV near the cage.

Using the computed potential and the dynamical equations, we can calculate the trajectories. Figure 6-9(a) shows the trajectories, where the point of emission for each electron is chosen randomly on the surface of the filament. As in the previous case, the initial energy of the emitted electrons does not affect the trajectories due to the strong fields involved. The new design does give a much smaller focus. The price to be paid is in the loss of several of the emitted electrons as they strike the cage walls. In the old design, almost all the emitted electrons made it to the target. However,

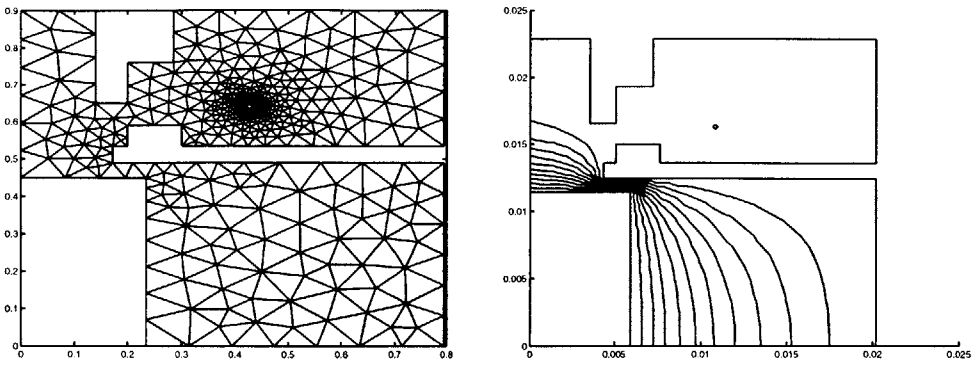

Figure 6-8: (a) Generated mesh for the new design. (b) The computed potential contours. The axis markers are in inches.

this loss is acceptable as long as the electron density in the focus on the target surface increases. Figure 6-9(b) shows the number of electrons striking the target surface. The focus is much smaller and the electron density is much higher than in the old design. Thus, we should expect a higher x-ray flux output.

We have built and used a simulation tool to study various designs for the electron-bombardment x-ray source. The proposed design predicts about 2.5 times increase in the x-ray flux. It also seems to produce a focal spot of about half the size of that in the existing design. Care should be taken while designing the target cooling system because of the small focus and high heating involved. Actual machining and experimental verification of the predictions need to be carried out in the future.

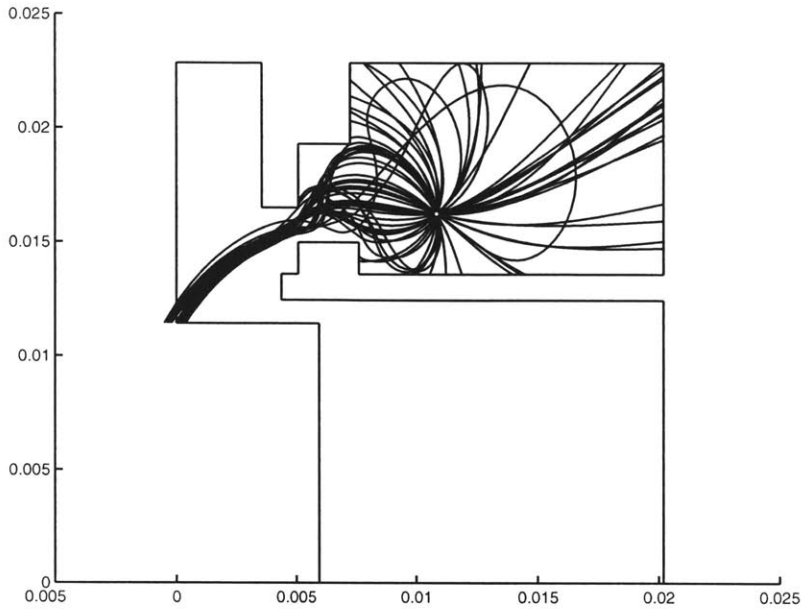

(a)

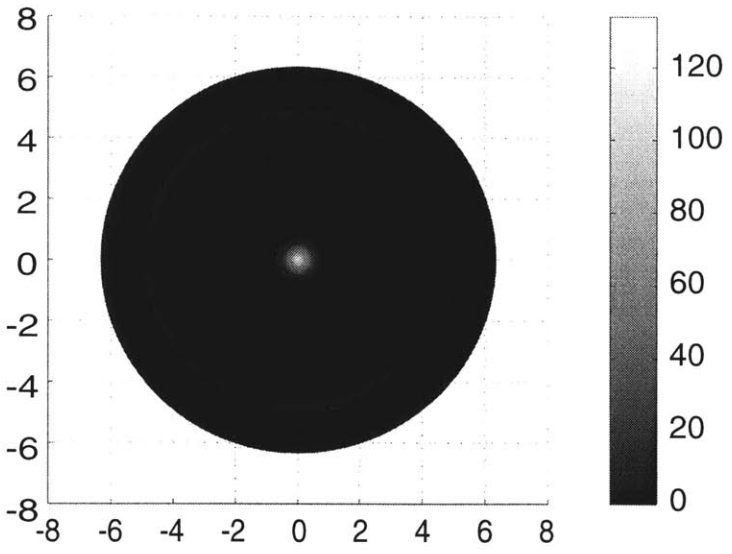

(b)

Figure 6-9: (a)Computed trajectories for the new design. The axis markers are in inches (b) Number of electrons striking the target surface. The focus is much smaller and the electron flux is much higher. The spatial dimensions are in mils. The graybar gives the actual number of electrons.

Chapter 7

Conclusions and Recommendations

A suite of simulation tools was developed to study the diffraction properties of zone plates in the context of ZPAL. The intensity near the focus of the zone plates was computed, and the effects of the various source and zone plate parameters were studied. zone plate fabrication errors were also considered. Using the focal intensity information, several patterns were simulated. These were compared to patterns exposed in resist and found to be in good agreement. Software to translate high-level kic diagrams to a format which can be used by the ZPAL system was written, and was used to perform the parallel patterning exposures in UV ZPAL. Finally, a simulator to study the electrodynamics in an electron-bombardment x-ray source was built. A new design for the x-ray source was proposed which would produce higher x-ray flux and a smaller source size.

The next stage of the research calls for the creation of a full vector diffraction simulator. This is especially important when lateral dimensions of the structures on the diffractive lenses are less than the wavelength. Finite-difference time-domain techniques seem to be the method of choice among many researchers to study diffractive lenses. This will enable the study of polarization induced effects, diffraction by sub-wavelength structures, and design of better diffractive lenses for ZPAL. These diffractive lenses then need to be fabricated and their properties tested. Another important future research thrust is in the pattern placement and linewidth control problems in ZPAL. These need to be addressed with grayscale techniques. Algorithms

need to be developed to automatically compute the necessary grayscale values for any desired pattern. The experience gained to date using the Fresnel-Kirchhoff diffraction model has given us confidence that a full vector model will provide valuable insight. Further analysis will likely result in the design of improved diffractive elements.

Appendix A

Overview of System Software

There is much system software design involved in the process starting from the concept of a pattern in a user's mind to actual exposed patterns on a wafer. We have touched some of the processes earlier. In this section, we will logically follow the process and elucidate the issues. A broad flow-chart of the different processes are illustrated in Figure A-1.

As mentioned earlier, the idea for a pattern is converted into a drawing using a CAD software tool such as the Nanowriter. The data is stored in the kic format. We need to convert this to a format which is more suitable for the ZPAL system. Translation software called *Kictozpal* was written in C to interpret the pattern in kic format and convert it into a more suitable form. The steps involved in the conversion are detailed next.

1. Inputs necessary for the interpretation are obtained. These include the pixel-size (`pixel_size`), the field-size in the x-direction (`field_size_x`), the field-size in the y-direction (`field_size_y`), the number of zone plates in the x-direction (`array_size_x`), the number of zone plates in the y-direction (`array_size_y`), a scaling factor used in Nanowriter (`lambda`) and the top-left corner coordinates of the pattern. The scaling factor is an input in Nanowriter, which scales every pixel value. This is important in order to prevent round-off errors and avoid fractional values for pixel coordinates. In the ZPAL coordinate system, the Y-axis is increasing in the downward direction. Hence, we need to shift the origin to the top-left corner of the

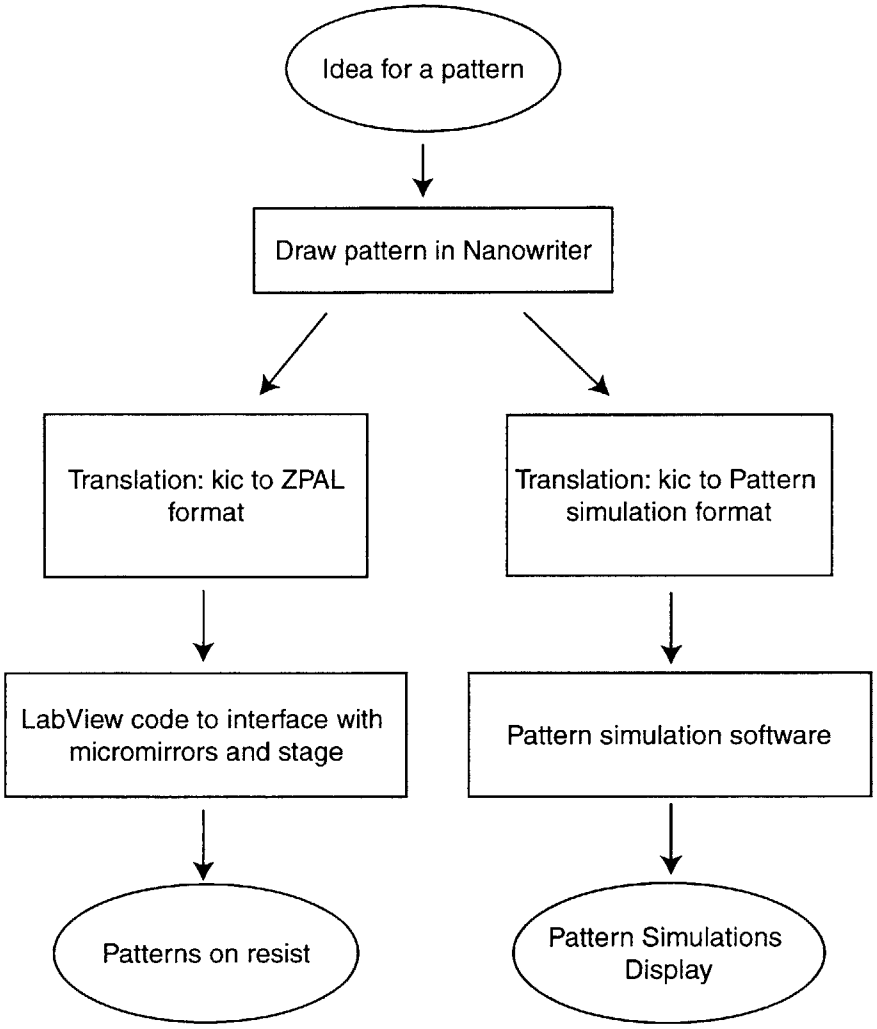

Figure A-1: Flow chart of process starting from the conception of the idea of a pattern to the actual attainment of the pattern on resist on a wafer and simulations of those patterns.

pattern. These inputs are used to define the zone-plate unit cells in pixel values.

2. The data from the kic file is read in. The data is in the form of boxes and they are in the format: `B width_x width_y center_x center_y`. This data is then interpreted in the actual scaled pixel values.

3. Every pixel in the pattern is checked to see if it lies within a drawn box and these are tagged. Here, overlapping boxes are checked to avoid multiple exposures. Also unexposed pixels are eliminated.

4. The pixel and exposure data are written to a file in the format: `Pixel_x Pixel_y B1 B2 ...`, where Pixel_x and Pixel_y are the x and y coordinates of the exposed pixel (the origin is the top-left corner of each unit cell), and B1, B2, ... are the bit values (1 if exposed and 0 if not) in the 1st, 2nd, ... unit cells. The data is written in a serpentine fashion.

The next step in the process is the control of the stage and micromirrors. This is done by using code written in LabView. The data in ZPAL format is read in. In the system, one micromirror addresses one zone plate. Hence, the bit values are used to signal the on-off state of the micromirrors. The X and Y pixel values control the motion of the stage. The data is ordered in such a manner that the stage implements a serpentine scan, which optimizes the writing time.

Appendix B

X-ray Source Measurements

* All dimensions from Head 2 (in inches)
* Target (gray center) is at ground and all other parts are at 5-8 keV
* Filament current ~ 15 A
* Height of target is varied to focus the spot

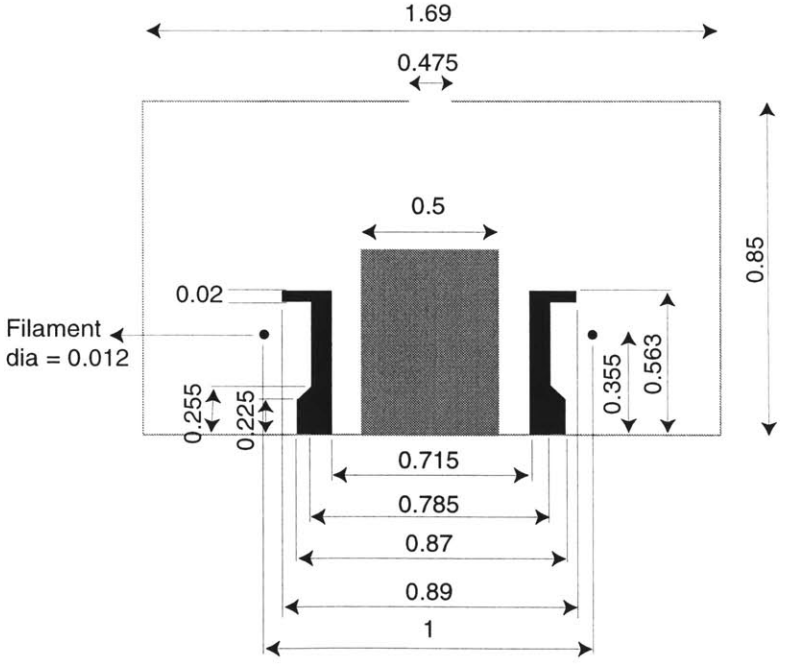

Figure B-1:

Bibliography

[1] Henry I. Smith. A proposal for maskless, zone-plate-array nanolithography. *J. Vac. Sci. Technol. B*, 14(6):4318–4322, Nov/Dec 1996.

[2] Ihsan J. Djomehri, T. A. Savas, and Henry I. Smith. Zone-plate-array lithography in the deep UV. *J. Vac. Sci. Technol. B*, 16(6):3426–3429, Nov/Dec 1998.

[3] Ihsan J. Djomehri. Zone plate array lithography in the deep UV. Master's project, Massachusetts Institute of Technology, Department of Electrical Engineering and Computer Science, September 1998.

[4] D. J. D. Carter, Darío Gil, Rajesh Menon, Ihsan J. Djomehri, and Henry I. Smith. Zone-plate-array lithography (ZPAL): A new maskless approach. In Yuli Vladimirsky, editor, *Emerging Lithographic Technologies III*, number 17 in Proceedings of SPIE, pages 133–139, Santa Clara, CA, March 1999. SPIE-The International Society for Optical Engineering.

[5] D. J. D. Carter, Darío Gil, Rajesh Menon, Mark K. Mondol, Erik H. Anderson, and Henry I. Smith. Maskless, parallel patterning with zone-plate array lithography. *J. Vac. Sci. Technol. B*, 17(6):3449–3452, Nov/Dec 1999.

[6] Rajesh Menon, D. J. D. Carter, Darío Gil, and Henry I. Smith. Zone-plate-array lithography (ZPAL): Simulations for system design. Presented at the VIth International Conference on X-ray Microscopy, Berkeley, CA August 1-6, 1999.

[7] D. J. D. Carter, Darío Gil, Rajesh Menon, and Henry I. Smith. Maskless nano-lithography with diffractive optics: Zone-plate-array lithography (ZPAL). Submitted to Diffractive Optics and Microfabricated Optics 2000.

[8] Henry I. Smith, D. J. D. Carter, M. Meinhold, E. E. Moon, M. H. Lim, J. Ferrera, M. Walsh, D. Gil, and R. Menon. Soft x-rays for deep sub-100 nm lithography, with and without masks. Presented at the Micro and Nano Engineering 99, Rome - September 21-23, 1999. To be published in Microcircuit Engineering.

[9] Lord Rayleigh. Wave theory. In *Encyclopaedia Brittanica*, page 429. Ninth edition, 1988.

[10] J. Soret. Über die durch kreisgitter erzeugten diffraktionsphänomene. *Annalen der Physik und Chemie*, 156:99–113, 1875.

[11] Alan G. Michette. *Optical Systems for Soft X Rays.* Plenum Press, 1986.

[12] Darío Gil. Maskless parallel patterning with zone plate array lithography (zpal). Master's project, Massachusetts Institute of Technology, Department of Electrical Engineering and Computer Science, June 2000.

[13] Gerd Schneider. *High-Resolution X-ray Microscopy of Radiation Sensitive Material.* Habilitationsschrift, Georg-August-Universität Göttingen, Forschungseinrichtung Röntgenphysik, Göttingen, 1999.

[14] D. C. Shaver, D. C. Flanders, N. M. Ceglio, and Henry I. Smith. X-ray zone plates fabricated using electron-beam and x-ray lithography. *J. Vac. Sci. Technol.*, 16(6):1626–1630, Nov./Dec. 1979.

[15] David Attwood. *Soft X-rays and Extreme Ultraviolet Radiation: Principles and Applications.* Cambridge University Press, 2000.

[16] J.W. Goodman. *Introduction to Fourier Optics.* Mc-Graw Hill, New York, 1996.

[17] M. Born and E. Wolf. *Principles of Optics.* Pergamon, New York, 1980.

[18] E. Hecht. *Optics.* Addison-Wesley, 1987.

[19] Cornell Theory Center, Cornell University, Ithaca, New York. World Wide Web (URL: `http://www.tc.cornell.edu/`).

[20] Roy D. Williams Geoffrey C. Fox and Paul C. Messina. *Parallel Computing Works.* Morgann Kauffmann Publishers Inc., 1994.

[21] Maui High Performance Computing Center, The University of New Mexico, Maui, Hawaii. World Wide Web (`URL:http://aixport.sut.ac.jp/advsys/mhppc/ibmhwsw/ibmhwsw.html/`).

[22] Private communication, David Foss, Research Laboratory for Electronics, MIT..

[23] IBM Corporation, Kingston, NY. *Engineering and Scientific Subroutine Library V2 R2. Guide and Reference*, 1994.

[24] William T. Vetterling William H. Press, Saul A. Teukolsky and Brian P. Flannery. *Numerical Recipes in C. The Art of Scientific Computing.* Cambridge University Press, 1997.

[25] Phillip J. Davis and Phillip Rabinowitz. *Methods of Numerical Integration.* Academic Press Inc., 1984.

[26] Henry I. Smith. *Lecture notes for course 6.781: Submicron and Nanometer Structures Technology.* NanoStructures Press, 1994.

[27] Henry I. Smith and D. C. Flanders. X-ray lithography - a review and assessment of future applications. *J. Vac. Sci. Technol.*, 17(1):533–535, Jan/Feb 1980.

[28] L. E. Ocola and F. Cerrina. Parametric modeling of photoelectron effects in x-ray lithography. *J. Vac. Sci. Technol. B*, 11(6):2839–2834, Nov/Dec 1993.

[29] T. Schliebe and G. Schneider. Zone plates in nickel and germanium for high-resolution x-ray microscopy. In Jürgen Thieme, Günter Schmahl, Dietbert

Rudolph, and Eberhard Umbach, editors, *X-ray Microscopy and Spectromicroscopy*, Status report from the Fifth International Conference, Würzburg, August 19-23, 1996, pages IV–1 – IV–12, Berlin, 1998. Springer-Verlag.

[30] T. D. Beynon and R. M. R. Strange. Computational study of diffraction patterns for near-field fresnel and gabor zone plates. *J. Opt. Soc. Am. A*, 17(1):101–106, January 2000.

[31] Drew A. Pommet, M. G. Moharam, and Eric B. Grann. Limits of scalar diffraction theory for diffractive phase elements. *J. Opt. Soc. Am. A*, 11(6):1827–1834, June 1994.

[32] M. G. Moharam and T. K. Gaylord. Diffraction analysis of surface-relief gratings. *J. Opt. Soc. Am.*, 72:1385–1392, 1982.

[33] Jörg Maser and Günter Schmahl. Coupled wave description of the diffraction by zone plates with high aspect ratios. *Optics Communications*, 89:355–362, 1992.

[34] Dennis Prather and Shouyuan Shi. Formulation and application of finite-difference time-domain method for the analysis of axially symmetric diffractive optical elements. *J. Opt. Soc. Am. A*, 16(5):1131–1142, May 1999.

[35] Scott D. Hector. *Optimization of Image Formation in X-Ray Lithography using Rigorous Electromagnetic Theory and Experiments.* Phd dissertation, Massachusetts Institute of Technology, MIT, Cambridge, MA 02139, 1994.

[36] David John Donat Carter. *Sub-50nm X-ray Lithography with Application to a Coupled Quantum Dot Device.* Phd dissertation, Massachusetts Institute of Technology, MIT, Cambridge, MA 02139, 1998.

[37] Euclid E. Moon. Dynamic nanometer alignment for nanofabrication and metrology. Master's project, Massachusetts Institute of Technology, Department of Electrical Engineering and Computer Science, September 1998.

[38] David J. Griffiths. *Introduction to Electrodynamics.* Prentice Hall, 1989.

[39] The Mathworks Inc., Natick, MA. *Partial Differential Equations Toolbox User's Guide*, 1999.

[40] Thermionic Emission, Class notes for Surface Science MS722 - EP733, University of Virginia. World Wide Web (`URL:http://bohr.ms.virginia.edu/bohr/surface/thermion.html`).